# Calibrating a Viscoelastic Sea Ice Model for Wave Propagation in the Arctic Fall Marginal Ice Zone

Sukun Cheng[1], W. Erick Rogers[2] (iD), Jim Thomson[3] (iD), Madison Smith[3] (iD), Martin J. Doble[4] (iD), Peter Wadhams[5] (iD), Alison L. Kohout[6], Björn Lund[7] (iD), Ola P.G. Persson[8], Clarence O. Collins III[9] (iD), Stephen F. Ackley[10], Fabien Montiel[11], and Hayley H. Shen[1] (iD)

[1]Department of Civil and Environmental Engineering, Clarkson University, Potsdam, NY, USA, [2]Naval Research Laboratory, Stennis Space Center, MS, USA, [3]Applied Physics Laboratory, Civil and Environmental Engineering, University of Washington, Seattle, WA, USA, [4]Polar Scientific Ltd, Appin, UK, [5]Department of Applied Mathematics and Theoretical Physics, University of Cambridge, Cambridge, UK, [6]National Institute of Water and Atmospheric Research, Christchurch, New Zealand, [7]Department of Ocean Sciences, University of Miami, Miami, FL, USA, [8]NOAA/ESRL Physical Sciences Division, Boulder, CO, USA, [9]Field Research Facility, Coastal and Hydraulics Laboratory, U.S. Army Engineering Research and Development Center, Duck, NC, USA, [10]Department of Geological Sciences, University of Texas at San Antonio, San Antonio, TX, USA, [11]Department of Mathematics and Statistics, University of Otago, Dunedin, New Zealand

**Abstract** This paper presents a wave-in-ice model calibration study. Data used were collected in the thin ice of the advancing autumn marginal ice zone of the western Arctic Ocean in 2015, where pancake ice was found to be prevalent. Multiple buoys were deployed in seven wave experiments; data from four of these experiments are used in the present study. Wave attenuation coefficients are calculated utilizing wave energy decay between two buoys measuring simultaneously within the ice covered region. Wavenumbers are measured in one of these experiments. Forcing parameters are obtained from simultaneous in-situ and remote sensing observations, as well as forecast/hindcast models. Cases from three wave experiments are used to calibrate a viscoelastic model for wave attenuation/dispersion in ice cover. The calibration is done by minimizing the difference between modeled and measured complex wavenumber, using a multi-objective genetic algorithm. The calibrated results are validated using two methods. One is to directly apply the calibrated viscoelastic parameters to one of the wave experiments not used in the calibration and then compare the attenuation from the model with measured data. The other is to use the calibrated viscoelastic model in WAVEWATCH III® over the entire western Beaufort Sea and then compare the wave spectra at two remote sites not used in the calibration. Both validations show reasonable agreement between the model and the measured data. The completed viscoelastic model is believed to be applicable to the fall marginal ice zone dominated by pancake ice.

## 1. Introduction

Rapid reduction of sea ice has significantly increased Arctic wave intensity (Thomson & Rogers, 2014) and facilitated the growth of shipping and offshore activities (Melia et al., 2016; Palmer & Croasdale, 2012). Forecast tools are needed to manage both marine and coastal operations against wave induced hazards. From previous observations, remote sensing or in-situ, it is known that wave propagation through ice covers is different from wave propagation in open water. As waves enter ice-covered waters, their speed changes, their amplitude attenuates and their energy scatters. For a relatively homogeneous cover, change of speed and attenuation are expected to dominate and may be described by a complex dispersion relation, where the real part of the wavenumber determines the wave speed, and the imaginary part of the wavenumber determines the amplitude attenuation. Several different dispersion models that relate this complex wavenumber to frequency and ice properties have been developed since the late nineteenth century (Squire, 2007, a review; Mosig et al., 2015, a more contemporary view). The predicted wave characteristics through an ice cover differ significantly between models.

Testing these theories is challenging because it requires simultaneous measurements of the meteorological condition, ice cover and the wave properties. Some studies using remote sensing data alone, or in conjunction with field measurements, have been performed (e.g., Wadhams & Holt, 1991; Wadhams et al., 2002,

2004). Field studies of wave propagation through ice cover have been few. Early reports began with casual observations from seafarers. Quantitative records of wave attenuation in ice covered ocean started to appear in the 1940s. A review of these early efforts may be found in Wadhams (1986). The early field studies focused on the fact that waves could penetrate an ice cover over a surprisingly long distance. With improved observational tools, both in-situ and remote sensing, the evolution of wave characteristics through ice covers has been documented in later field studies. The two most important findings from these more recent field studies are: frequency dependent wave attenuation (Wadhams et al., 1988), and directional spreading of wave energy (Wadhams et al., 1986). With growing awareness of the importance of sea ice on the global climate system, field studies investigating wave-ice interaction in polar regions have increased. Recent studies include Kohout et al. (2014) and Doble et al. (2015) with data collected in the Southern Ocean. They used buoys either riding on top of ice floes or drifting amongst ice floes to directly measure the wave attenuation. By leaving the buoys drifting with the ice over several days to weeks, the datasets captured episodes of different wave events. These studies clearly showed frequency dependent attenuation and penetration of waves more than several hundreds of kilometers into an ice cover, particularly under stormy conditions (Kohout et al., 2014; Meylan et al., 2014). A number of shorter duration field studies in different parts of the polar regions also demonstrated selective wave attenuation (e.g., Collins et al., 2015; Frankenstein et al., 2001; Squire & Moore, 1980).

Theory for wave propagation in ice-covered waters began with assuming ice as a pure elastic floating plate (Greenhill, 1887), followed by the mass-loading model (Peters, 1950; Weitz & Keller, 1950), the pure viscous layer model (De Carolis & Desiderio, 2002; Keller, 1998), and the viscoelastic model (Squire & Allan, 1980; Wadhams, 1973; Wang & Shen, 2010). All of the above theories consider ice cover as a continuum, whose deformation is governed by its constitutive behavior. Different ice mechanical assumptions among some of these models cause wave shortening or lengthening, as shown in a study of surveying models and field data (Collins et al. 2017). The continuum theories focus on the attenuation/dispersion process. By expanding on the pure elastic plate theory, models for wave scattering through a field of discrete ice floes have also been developed (Squire, 2011 and references therein; Squire & Montiel, 2016).

All of the theoretical models were established based on heuristic assumptions. As for general composite materials, it is expected that no single idealized model can precisely describe all types of ice covers. It is thus desirable to construct an ice model that captures the most essential properties that affect wave propagation. Different viscoelastic models were considered based on this premise. In this study, we focus on one such model (Wang & Shen, 2010), which was shown to converge to each previously proposed model under proper limiting conditions: thin elastic plate, mass loading, and pure viscous layer. This viscoelastic model assumes that all ice covers possess some energy storage ability that can be described by an equivalent elasticity, and a dissipative ability that can be described by an equivalent viscosity. This model has been used in wave hindcasts and compared reasonably well with field data from the Antarctic (Li et al., 2015), and the Arctic (Rogers et al., 2016). It has been included in the global wave model WAVEWATCH III ® (WW3) (Tolman & the WAVEWATCH III® Development Group, 2016) as one of the possible modules to describe the effects due to ice covers. The greatest challenge of applying this model is the unknown equivalent elastic and viscous parameters. To derive these mechanical parameters from first principles is unfeasible, even for simple fluids. The alternative is to determine these parameters through calibration with measured data. In this paper, we use field data to calibrate these model parameters. The data are from the SeaState and Boundary Layer Physics of the Emerging Arctic Ocean (SeaState) field campaign, conducted 30 September to 4 November, 2015 in the Chukchi-Beaufort Seas and the western Arctic Ocean aboard R/V Sikuliaq (SKQ) (Thomson, 2015; Wadhams & Thomson, 2015).

The basic idea of using the SeaState data to calibrate the viscoelastic wave dispersion model was illustrated in Cheng et al. (2016), in which four pairs of buoy time series were used. In the present study the full buoy datasets are analyzed. After systematic filtering, several hundred pairs of time series are utilized. Moreover, careful selection of the ice and wind data among many readily available sources is made to facilitate the calibration. A more efficient optimization scheme is used to handle the large number of cases.

This paper is organized as follows: Section 2 briefly describes the viscoelastic model. Section 3 describes the relevant datasets obtained from the field campaign, and criteria used to narrow down the datasets for

calibration. Section 4 describes the measured attenuation from all selected buoy pairs. Section 5 provides the procedure and the results of the calibration. Model validation is discussed in section 6. Final remarks and recommendations for further study are given in section 7. Data sources and comparisons of various observations, such as atmospheric and ice characteristics, are presented in the supporting information to motivate the choices for the model input of key parameters.

## 2. Theoretical Background

In deep water, wave propagation through an ice-covered sea is governed by the energy balance equation

$$\frac{\partial F(f, \theta)}{\partial t} + \nabla_{\mathbf{x}} \cdot \mathbf{c_g} F(f, \theta) = S_{in} + S_{ds} + S_{nl} + S_{ice} \tag{1}$$

where $F(f, \theta)$ is the spectral energy density, $\mathbf{c_g}$ is the group velocity, $S_{in}$ the wind input, $S_{ds}$ the dissipation through wave breaking, $S_{nl}$ the energy transfer due to nonlinear interactions among spectral components, and $S_{ice}$ the damping due to ice cover. Many other terms, such as sea-bed friction, are irrelevant to this study and hence omitted here. In an ice covered region, following Komen et al. (1994), Perrie and Hu [1996], and the WW3 manual (version 4 and later) (Tolman & the WAVEWATCH III® Development Group, 2016), $S_{in}$ and $S_{ds}$ are scaled by the open water fraction, while $S_{ice}$ is scaled by the ice concentration, $C$. $S_{nl}$ is the same as in open water. Thus in an ice covered region, equation (1) is modified as

$$\frac{\partial F(f, \theta)}{\partial t} + \nabla_{\mathbf{x}} \cdot \mathbf{c_g} F(f, \theta) = (1 - C)(S_{in} + S_{ds}) + S_{nl} + C S_{ice} \tag{2}$$

For an open ocean, both $C$ and $S_{ice}$ are equal to zero. The rest of the terms in equation (2) have been calibrated with extensive field data during and since the JONSWAP project (Hasselmann et al., 1973). Prior to the SeaState program reported in this special issue, most of the wave data for ice-covered seas were from the MIZEX project (Kramer, 1996, Appendix A) and a handful of field experiments as mentioned earlier. In the present study, SeaState data are used to determine the source term $S_{ice}$ and the group velocity $\mathbf{c_g}$ in equation (2). Models of the other source terms remain the same as detailed in the most recent WW3 manual (Tolman & the WAVEWATCH III® Development Group, 2016).

At present WW3 contains several modules to treat $S_{ice}$, each based on a different concept. The first module, IC0, provides simple blocking of energy flux from one computational cell to the next, depending on the local ice concentration (Tolman, 2003). IC1 lets the user choose a constant attenuation coefficient for all wave frequencies. IC2 is based on damping due to the turbulence boundary layer under the ice cover (Liu & Mollo-Christensen, 1988). IC3 assumes ice cover as a linear viscoelastic continuum (Wang & Shen, 2010). Finally, IC4 uses parameterized attenuation from direct fitting with field data (Collins & Rogers, 2017). Scattering is also included in this most recent WW3 release as modules IS1 and IS2.

In this study, we focus on IC3, which has two parameters related to the mechanical properties of an ice cover: equivalent elasticity and equivalent viscosity. The theoretical basis for IC3 is described in details in the original reference (Wang & Shen, 2010). Here we extract the most essential parts of this theory to illustrate the concept. The linkage between IC3 and $S_{ice}$ is discussed in section 5.

Imagine an ice cover consisting of any variety of ice types: frazil, pancake, floes of various sizes, or a semicontinuous ice sheet with cracks, rafts, and ridges. As a train of wave passes through it, this ice cover deflects. Along with the deflection, some wave energy is stored, either in the form of gravity potential (if the part of ice cover behaves as a rigid body) or elasticity (if the part of ice is deformable), and some energy is dissipated. The elastic energy stored depends not only on the intrinsic elasticity of the ice floes, but also on its size. Small floes in large waves bend little, hence the stored elastic energy is less than larger floes of the same property. The existence of an "equivalent" elastic modulus was shown in a laboratory experiment (Sakai & Hanai, 2002). In which, the wave celerity through a floating polyethylene sheet with a known Young's modulus was measured against predictions from the thin elastic theory (Fox & Squire, 1994). Agreement was obtained at full length. They then cut the sheet into successively smaller segments keeping the full length unchanged. The results show a consistently decreasing celerity corresponding to reduction of an equivalent elasticity for the assembly of floes. Theoretical derivations of the equivalent elasticity for an assembly of floating discrete elastic body await further study. Energy dissipation in an ice cover can be due

to a variety of processes such as the viscosity of frazil crystals that render the ice cover as a slurry; inelastic bumping of ice floes with each other; inelastic deformation; drag of ice floes moving relative to the surrounding frazil or pure water. The internal stress of the ice cover can therefore be described by the combination of these two types of processes: storage and dissipation. Provided that the storage depends on the deformation and dissipation depends on the rate of deformation, the simplest model for the combined stress is the linear viscoelastic model,

$$\tau_{mn} = -P\delta_{mn} + 2GS_{mn} + 2\rho_{ice}v\dot{S}_{mn} \tag{3}$$

where $\tau_{mn}$, $S_{mn}$ and $\dot{S}_{mn}$ represent the stress tensor, the strain and strain rate tensor, respectively; $m$ and $n$ represent horizontal or vertical direction. $G$ and $v$ are the effective shear modulus and the effective kinematic viscosity of the ice layer, respectively; $P$ is the pressure and $\delta_{mn}$ the Kronecker delta. Such model is called the Voigt model if $G$ and $v$ are constants (Meyers & Chawla, 2008). In fact, this assumption can be relaxed so that $G$ and $v$ depend on wave frequency without affecting the resulting dispersion relation, as long as we are in the linear wave regime (Mei et al., 2010). For a given angular frequency, $\sigma$, this model yields the velocity potential, $\phi \sim e^{i(kx-\sigma t)}$, of the wave field through the ice cover. Here, the complex wavenumber $k = k_r + ik_i$ is determined by the dispersion relation described later. The real part, $k_r$, is the physical wavenumber needed to determine the group velocity $c_g = d\sigma/dk_r$. The imaginary part, $k_i$, is the attenuation coefficient for the wave amplitude, $A$, so that $\frac{\partial A}{\partial x} = -k_i A$. An exponential damping is a natural characteristic of this model. The resulting wave dispersion relation may be put concisely as

$$\sigma^2 - Q_c gk\tanh kH = 0 \tag{4a}$$

where $H$ is the water depth and

$$Q_c = 1 + \frac{\rho_{ice}}{\rho_{water}} \frac{g^2 k^2 S_k C_\alpha - (N^4 + 16k^6\alpha^2 v_e^4)S_k S_\alpha - 8k^3\alpha v_e^2 (C_k C_\alpha - 1)}{gk(4k^3\alpha v_e^2 S_k C_\alpha + N^2 S_\alpha C_k - gkS_k S_\alpha)} \tag{4b}$$

In the above, $S_k = \sinh kh$, $S_\alpha = \sinh\alpha h$, $C_k = \cosh kh$, $C_\alpha = \cosh\alpha h$, $N = \sigma + 2ik^2 v_e$, $\alpha^2 = k^2 - \frac{i\sigma}{v_e}$, and $v_e = v + \frac{iG}{\rho_{ice}\sigma}$. The ice cover thickness is $h$. $\rho_{ice}$ and $\rho_{water}$ are densities of ice and water, respectively. This dispersion relation has many wave modes; the gravity wave mode selected in this study is the one that corresponds to the observable propagating wave (Zhao et al. 2017). We used $\rho_{ice} = 917$ kg/m³, $\rho_{water} = 1,025$ kg/m³ and deep water condition throughout this study, appropriate to the field conditions encountered by the buoys. The ice thickness is from measurements to be described in section 3.

Once the ice properties are known, the wavenumber $k$ may be determined for each angular frequency $\sigma$ following equation (4). Everything else in equation (4) can be directly measured except the equivalent elasticity $G$ and viscosity $v$. The elastic modulus of an ice beam or plate may be measured with strain gauges under static and dynamic loading conditions (Timco & Weeks, 2010), but not a collection of floes mixed with frazil crystals or brash ice. Such a collection was prevalent in our field campaign (Thomson, 2015; Wadhams & Thomson, 2015). The strategy employed here is to inversely determine these two mechanical properties using measured $k$. Through minimizing the discrepancies between the measured and the theoretical $k$ obtained with equation (4), the optimized $G$ and $v$ are thus determined for the corresponding ice cover. For future wave forecasts, once the ice type is known either from remote sensing observations or from advanced ice modeling, the equivalent $G$ and $v$ may then be employed to determine $k$.

The inverse method has been used to determine the effective viscosity of grease ice (Newyear & Martin, 1999), in which they measured the wavenumber and attenuation of monochromatic waves through a layer of grease ice generated in a laboratory wave flume, and fit the data using the pure viscous theory of Keller (1998). In the laboratory, the situation is simpler because the absence of other source terms such as wind input, wave breaking and nonlinear energy transfer between frequencies. In the field, these other source terms may significantly affect the measured wave attenuation (Li et al., 2015). Despite the uncertainty contributed by other source terms, the inverse method has been used in field studies to determine the effective viscosity of a grease ice cover (Rabault et al., 2017) and a pancake ice cover (Doble et al., 2015). In the calibration work to be presented in section 5, two methods will be used and results compared. One ignores the other source terms and the other includes them. For the latter, wind information is needed. Both methods require wave spectra, ice thickness and concentration data.

## 3. The Data Sets

First we describe the general field conditions. Because all wave experiments were conducted in the marginal ice zone, the ice cover advanced and retreated dynamically during each wave experiment (Thomson et al., 2017). As an example, Figure 1 gives the general overview of the last wave experiment of this field campaign on 31 October to 1 November (Wave Experiment 7). The background satellite images provide a large view of the region. In panel (a) the background is a satellite image from RADARSAT-2 taken at the beginning of this period. In panel (b) an image from Sentinel-1 taken at the end of this period is shown. Comparing with panel (a), the ice edge in (b) retreated significantly within the day and half between the two images, leaving some buoys in open water by the end of this wave experiment. During this wave experiment, the ship followed a rectangular racetrack pattern to collect atmosphere and ocean fluxes at the ice edge (Thomson, 2015; Wadhams & Thomson, 2015). The deployed buoys were all initiated from this racetrack but drifted northwest (supporting information Figure S1). No intermediate imagery is available to better constrain the time of the ice retreat and the ice conditions for each buoy.

There are several relevant datasets needed for this study: the wave, the ice, and the wind.

### 3.1. Wave Data

From 30 September to 4. November 2015 there were seven Wave Experiments (WE) performed: WE1 through WE7 (map shown in Thomson (2015) and Wadhams & Thomson (2015)). WE1, 2, and 5 are not used in this study; WE1 was performed in open water to check all wave buoys and WE2 and 5 were short deployments with only a few buoys. The time and location of the WEs were determined by wave and wind conditions, with a guiding principle to capture large wave events and to cover both on-ice and off-ice wind conditions. Details of these deployments are given in Thomson (2015) and Wadhams and Thomson (2015). Key variables in this study measured by SWIFT and WB buoys of WE3, 4, 6, and 7 are summarized in Table 1, including the spatial coverage, typical wave direction and height, and representative wind direction and speed. The values shown in this table are averages in each WE (supporting information Figures S1–S5). For the present study, we use WE3, 6, and 7 to perform the calibration in section 5. WE4 and part of WE3 data are then used in the model validation to be discussed in section 6.

Three types of drifting wave buoys were used in the SeaState field campaign: SWIFT (Thomson, 2012), WB (Doble et al., 2015), NIWA buoy – a variant from its predecessor WIIOS (Kohout et al., 2015). There were six SWIFTs, ten WBs, and one NIWA buoy available in this field study, though not all of them were deployed in each WE. All buoy data were split into 30-min segments and then post-processed to obtain the directional spectra using method given in Thomson (2012). SWIFT data cover the frequency interval (0.0566, 0.4902) Hz with an increment of 0.0117 Hz, while WB data cover (0.0557, 0.4951) Hz with an increment of 0.0098 Hz. To
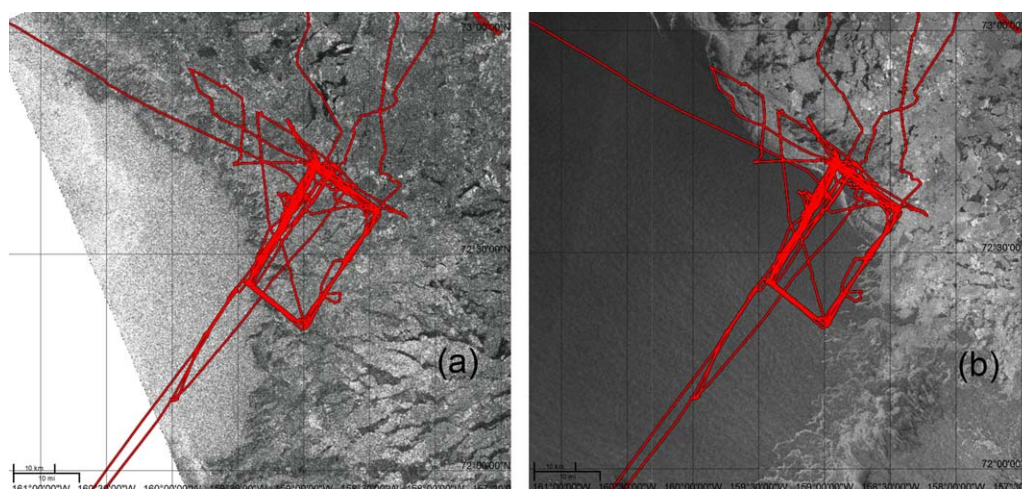


**Figure 1.** Images of ice condition over the study region. Red line is the ship track from the start of the cruise. Background image taken: (a) 31 October, 03:22 UTC from RADARSAT-2; (b) 1, November, 17:23 UTC from Sentinel-1. During this time the ship followed a racetrack pattern to capture fluxes in the atmosphere and the ocean at the ice edge.

**Table 1**
*Summary of Time Span, Location, Wave and Wind Information, and Buoys Deployed for Each WEa*

| WE No. | Duration (2015) | Mean location | R (km) | Wad | Hs (m) | Wid | Wis (m/s) | Deployed buoys |
|---|---|---|---|---|---|---|---|---|
| 3 | 10–13, Oct. | 72.9°N, 150.5°W | 90 | S-SE | $\leq 5$ | E-SE | $\leq 18$ | S09, 11, 12, 13, 14, 15 WB 02, 03, 04, 05, 07, NIWA |
| 4 | 16–18, Oct. | 73.8°N, 162°W | 40 | SW | $\leq 0.5$ | SE | $\leq 5$ | S11, 12, 14, 15 WB 02, 03, 04, 06, 07, 09 |
| 6 | 23–24, Oct. | 72.6°N, 158.8°W | 30 | SE | $\leq 1.5$ | E-SE | $\leq 14$ | S09, 11, 12, 13, 14, 15 WB 02, 03, 06, 07, 09 |
| 7 | 31, Oct. – 1, Nov. | 72.7°N, 159.3°W | 20 | SW | $\leq 1.5$ | S-SE | $\leq 13$ | S09, 11, 13, 15 WB 02, 03, 06, 07, 08 |

*Note:* All directions follow the nautical convention. S08 and S10 were lost to the sea during WE3. Values shown are the averaged over data directly from sensors on SWIFT and WB buoys. Details of these data are given in Figures S1-S5 of the supporting information. R: Approximate spatial coverage of studied buoy pairs; Wad: Wave direction; Hs: significant wave height; Wid: Wind direction; Wis: wind speed. Wid and Wis are from SWIFT buoy at 1 m above water surface. Specific duration when buoys were in field: WE3: 10-Oct-2015 10:00:00 to 14-Oct-2015 02; WE4: 17-Oct-2015 00:30:00 to 18-Oct-2015 17:30:00; WE6: 23-Oct-2015 15:30:00 to 25-Oct-2015 05:00:00; WE7: 31-Oct-2015 16:30:00 to 01-Nov-2015 23:00:00.

be consistent, WB data are first interpolated onto the frequency domain of SWIFT prior to further analysis. Additional wave data from a Nortek Acoustic Wave and Current Meter (AWAC) mooring spanning the WE3 period will be used for model validation.

For each 30-min period, stationary conditions are assumed. As described in section 2, exponential attenuation is a natural consequence of the viscoelastic model adopted in this study. Thus, from a pair of 30-min directional spectra, at each frequency $f_j$, the apparent attenuation of wave amplitude between buoys $A$ and $B$ is

$$\alpha(f_j) = \frac{1}{2D_{AB}} \ln\left(\frac{F_A(f_j, \theta_{Aj})}{F_B(f_j, \theta_{Bj})}\right) \tag{5a}$$

$$D_{AB} = D\cos(\theta_j - \theta_{AB}) \tag{5b}$$

where $F_A(f_j, \theta_{Aj})$ and $F_B(f_j, \theta_{Bj})$ are the directional spectral energy density, with $\theta_{Aj}$, $\theta_{Bj}$ corresponding to the mean direction at $f_j$. $D$ is the distance from $A$ to $B$, and $\theta_{AB}$ is its vector direction. The average of the mean wave directions at $A$ and $B$, $\theta_j = \frac{\theta_{Aj} + \theta_{Bj}}{2}$, is used to estimate propagation distance for the wave component. Buoy $A$ is upstream in the peak wave direction. $F_A$, $F_B$ and $\alpha$ are smoothed with a five-point moving average in the frequency domain.

While calculating this apparent energy attenuation coefficient from the buoy data is straightforward, it is not straightforward to relate $\alpha$ to $k_i$ in equation (4). First, the ice concentration, $C$, between the two buoys must be accounted for. Second, there is not only damping due to ice between two buoys, but also other source terms mentioned earlier. It is straightforward to account for ice concentration by letting $\alpha = Ck_i$. In this way, $k_i$ is the apparent attenuation coefficient of the wave amplitude between two buoys assuming full ice coverage. In the above, all source/sink mechanisms other than from the ice cover are not considered. In section 5, we will call this method of calculating $k_i$ the 'simple' method. To account for other source/sink terms in equation (2), the 'full' method will also be adopted. Details and results of both methods will be shown in section 5.

### 3.2. Ice Data

A complete list of collected data sources is given in the supporting information. They may be classified into two types.

Along the ship track:

1. Hourly visual observations conducted aboard the ship using the ASSIST protocol (http://www.iarc.uaf.edu/icewatch), which provided three ice types, their partial concentrations and thickness estimates. These

were supplemented by occasional ship-side sampling of the ice cover retrieved manually ("dipnet" for pancakes and "frazilometer" for frazil ice);

2. 10-min average ice thickness from the Heitronics KT-15 infrared pyrometers mounted on the ship mast. The measured skin temperature, wind, ocean freezing point, and energy fluxes, are combined with surface energy budget equations to estimate ice thickness. This ship-based technique improves on related satellite-based algorithms used by Groves and Stringer (1991), Yu and Rothrock (1996), and Wang et al. (2010).

Regional:

3. The Los Alamos Sea Ice Model (CICE), as operated by the U.S. Navy (e.g., Hebert et al., 2015; Posey et al., 2015), provides daily ice thickness and concentration. This product (hereafter called N-CICE), through data assimilation, closely conforms to the sea ice mask produced by the National Ice Center (NIC);

4. Advanced Microwave Scanning Radiometer 2 (AMSR2), provides ice concentrations at irregular intervals four to five times a day at 10 km resolution. The data is produced using the NASA Team (NT2) algorithm (Markus & Cavalieri, 2000, 2009) developed for the predecessor instrument AMSR-E (Advanced Microwave Scanning Radiometer - Earth Observing System);

5. Soil Moisture and Ocean Salinity (SMOS) satellite, provides daily ice thicknesses. The data is inferred empirically from the brightness temperature, averaged over $40° \sim 50°$ incident angle (Huntemann et al., 2014).

6. Other regional ice concentration and thickness data from remote sensing have also been collected but not used in this study. They are listed in the supporting information.

Among all data collected for ice characteristics in the study region, the combination of AMSR2 (ice concentration) and SMOS (ice thickness) is in better agreement with the in-situ data along the ship track, according to the standard deviation and correlation coefficient of the regional datasets with respect to the Heitronics KT-15 infrared pyrometers on ship (supporting information Figures S6 and S7). The main results of this study to be discussed are from this combination of ice data. We also present results derived from N-CICE, since using both ice data sources provides a sensitivity measure for the calibration results. Furthermore, N-CICE was used in a previous study closely related to the present one (Rogers et al., 2016), which will be compared with in the discussion section. We summarize the ice data used in this study in Table 2. The ice morphology in Table 2 is from the hourly observation using the ASSIST protocol. Cases when the ship was in open water are first removed. The rest of data are organized into four categories, $i = 1$ to 4. The numbers shown are $\frac{C_{ct_1}}{Tc} / \frac{C_{ct_2}}{Tc} / \frac{C_{ct_3}}{Tc} / \frac{C_{ct_4}}{Tc}$, where $ct_i$ is the partial concentration of category $i$ and $Tc$ the total ice concentration. These categories from $i = 1$ to 4 are, respectively: thick (code 75, 80, 85, 95)/pancake (code 30)/thin (code 10–13, 20)/other (code 40–70, 90). Definition of these ice codes may be found at http://www.climate-cryosphere.org/media-gallery/881-icewatch-assist. Time series of the ice type in each WE's are given in the supporting information Figure S8.

### 3.3. Wind Data

There are also regional and in-situ data for the wind field. The regional data may be obtained from the European Centre for Medium-Range Weather Forecasts (ECMWF) (Andersson 2015) and the Navy Global Environmental Model (NAVGEM) (Hogan et al., 2014). The in-situ data are from the SWIFT buoy anemometers at 1 m height above the surface as well as the quality-controlled 16.5 m values obtained from the suite of shipboard anemometers. WB buoys do not have wind measuring instrument. Using nearby SWIFT wind data may cause bias when buoys were far apart, in addition to icing problem on buoy instrument to be discussed in section 4. A space-continuous wind data resource is required for this study. We thus choose NAVGEM, because it agrees well with in-situ data along the ship track (supporting information Figure S9).

### 4. The Measured Wave Characteristics

The real part of the wavenumber $k_r$ is determined by two independent methods. One applies the 'slope method' based on the cross-correlation of the heave-pitch-roll signal to estimate the low-order directional moments and an estimate of the root-mean-square wavenumber (Longuet-Higgins et al., 1963; Appendix A of Kuik et al.,
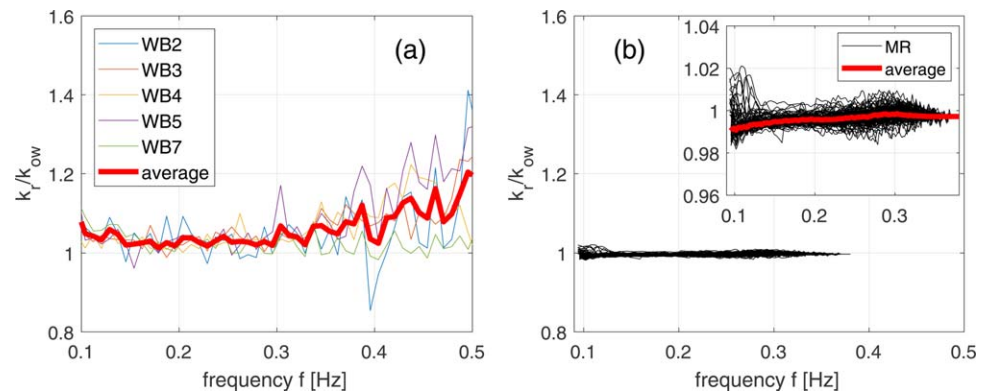
**Table 2**
*Ice Conditions in Each of the Wave Experiments*[a]

| WE No. | Ice thickness (m) | Ice concentration | Ice morphology |
|---|---|---|---|
| 3 | (0.01, 0.03] | [0.15, 0.55] | 0/0.59/0.41/0 |
| 4 | [0.08, 0.16] | [0.6, 1] | 0.06/0.59/0.13/0.23 |
| 6 | (0.01, 0.04] | [0.25, 0.5] | 0/0.43/0.27/0.29 |
| 7 | [0.03, 0.07] | [0.15, 0.6] | 0/0.23/0.13/0.64 |

[a]Ice products are from AMSR2 + SMOS and visual observations using ASSIST protocol.

**Figure 2.** Ratio of the estimated real wavenumber $k_r$ over open water wave number $k_{ow}$; (a) from the slope method, WB buoys; (b) from the MR; both from WE3, using a collection of 30-min mean datasets.

1988; Collins et al., 2014). This method is applied to the WB buoy datasets only, with formula given in the Appendix A, equation (A3). SWIFT buoys do not provide this estimate, because the hulls are not designed to measure sea surface angles of pitch or roll (Thomson, 2012). The other method uses the shipboard X-band Marine Radar (MR). This method has the advantage over most satellite-borne products in that it samples surface waves in space and time, therefore allowing a direct measurement of wave dispersion (Young et al., 1985). The datasets used in these two methods are not co-located. One followed the WB buoy tracks and the other the ship track. Both were in the same general area.

The estimated real part of the wavenumber, $k_r$, from the slope method and the MR images are given in Figure 2, where $k_{ow}$ is the open water wavenumber under deep water condition. Each curve shown represents the result from a 30-min mean dataset. The results from the slope method are widely scattered, but the average among buoys is close to the open water wavenumber with an upward trend at high frequencies. The MR results, which do not cover the high frequency part as in the slope method, are extremely close to the open water wavenumber and nearly flat with respect to frequency. This wavenumber analysis is presently only available for WE3.

To estimate $k_i$, the imaginary part of the wavenumber, we need to start from the apparent attenuation coefficient $\alpha$. In principle, any pair of buoys that were deployed during the same 30-min interval could be used to determine $k_i$. In practice, however, many of these pairs are not usable for various reasons. A set of filters is applied to select pairs of buoys for the attenuation analysis. The first layer of filters to apply to a pair of buoys $A$ and $B$ are:

1. Data from two buoys must be in the same 30-min period.
2. The measured waves must exceed a minimum height for a valid signal from both buoys. $Hs_A > Hs_B > 0.01$ m, $Hs_A - Hs_B > 0.02$ m, where Hs is the significant wave height.
3. The Pearson correlation coefficient of wave spectra of the two buoys must be greater than 0.4. Definition of this coefficient is given in the Appendix A.
4. The angle between the direction from buoy $A$ to buoy $B$, $\theta_{AB}$, and average of the two peak wave directions at $A$ and $B$, $\theta$, must be less than $90°$.
5. The Power Spectral Density (PSD) must exceed a minimum value from either buoy at frequency $f$, $S(f) = \int F d\theta > 10^{-5}$ m$^2$/Hz. Otherwise, this $f$ is deleted from further analysis.
6. The spectra check factor of either buoy at frequency $f$ must be less than 4. Definition of the spectra check factor is given in the Appendix A.
7. Each buoy pair that passed all above criteria must also have positive attenuation values $\alpha(f)$ at a minimum of 7 frequencies.

Furthermore, mixed pairs with one SWIFT and one WB buoy are excluded. Although including these mixed pairs would increase the sample size and thus more meaningful results statistically, consistency between buoy types must be ensured. SWIFT buoys are based on GPS method known to bias high in energy, especially at low frequencies (Herbers et al., 2012). Correction for this bias was done via post-processing to merge additional Inertial Measurement Unit data, and validated in open water conditions. Employing this

**Figure 3.** Photos of various ice conditions taken from ship bridge during WE3, 4, 6, and 7.

correction, in WE1 a cross-calibration between SWIFTs and WBs was performed successfully. However, in WE3, it was found that the two buoy types responded in similar manners at first, but their differences grew in time, with SWIFT reporting lower energy than WB, even when they were in close proximity of each other ($\sim$ 0.4 km). Icing resulted changes of hydrodynamic responses from these two types of buoys are suspected to be the reason for this discrepancy. SWIFTs are spar shaped while WBs are circular disks. The shape differences resulted in very different icing conditions. Changes of hydrodynamic response of buoys can alter the frequency response of a buoy, as studied in a biofouling case (Thomson et al., 2015). Without a thorough study of sources of the observed discrepancies between these two types of buoys, reliable cross-calibration cannot be performed. Hence in the following, no mixed pairs are included in the study. We note that this choice does not remove the possibility of different icing between pairs of buoys of the same type, which we believe would be much less than between different types of buoys. This is an uncertainty that we accept in the data.

The above seven filters is only the first layer of filters to select the potential candidates for calibration. In sections 4 and 5, additional filters are applied. For example, we will also require both buoys to be in an ice covered region. Of all combinations of SWIFTs and WBs, more than a thousand cases are selected after the above filters. Because the study area was in the marginal ice zone in the growth season, the ice conditions changed rapidly in time and space as the example shown in Figure 1. To visualize the diversity of in-situ ice conditions, Figure 3 shows multiple photos taken at the ship bridge from WE3, 4, 6 and 7. Various ice concentrations, thickness, and sea surface types are observed from mostly open water to pancake-frazil ice to first year ice floes. Time series of ASSIST-protocol ice concentration and ice type fractions are shown in supporting information Figure S8.

To study ice-induced wave attenuation, we need to exclude some pairs that were mostly in open water. Hence, a second layer of filters consisting two steps are applied here.

1. We select cases where the ice concentration from AMSR2 is equal to or greater than 15% and ice thickness from SMOS is equal to or greater than 1 cm.
2. Some cases that have passed pre-filters 4, 5, and 7, but only have positive $\alpha(f)$ in either low or high frequency bands. To avoid bias toward only low or high frequencies during calibration in section 5, we skip cases in which the number of positive $\alpha(f)$ in frequency interval [0.056, 0.3] Hz or [0.3, 0.49] Hz is less than 4. Through this filter, cases from WE4 are all skipped. Hence no calibration is performed for WE4, which will be used in section 6 for validating the calibrated results from WE3, 6, and 7.

Figures 4a and 4b show the corresponding $\alpha(f)$ of these selected cases based on the two layers of filters, respectively. The black lines represent data from SWIFTs and the grey lines represent data from WBs. Number of cases passed the above filters are marked in each WE. From the number of cases selected in Figure 4b, SWIFTs contribute more data in WE3, while WBs contribute more data in WE6 and 7.

The attenuation curves in Figure 4b are widely varied. However, the range and behavior of the attenuation curves from SWIFTs and WBs are similar, we thus do not distinguish them in the following analysis.
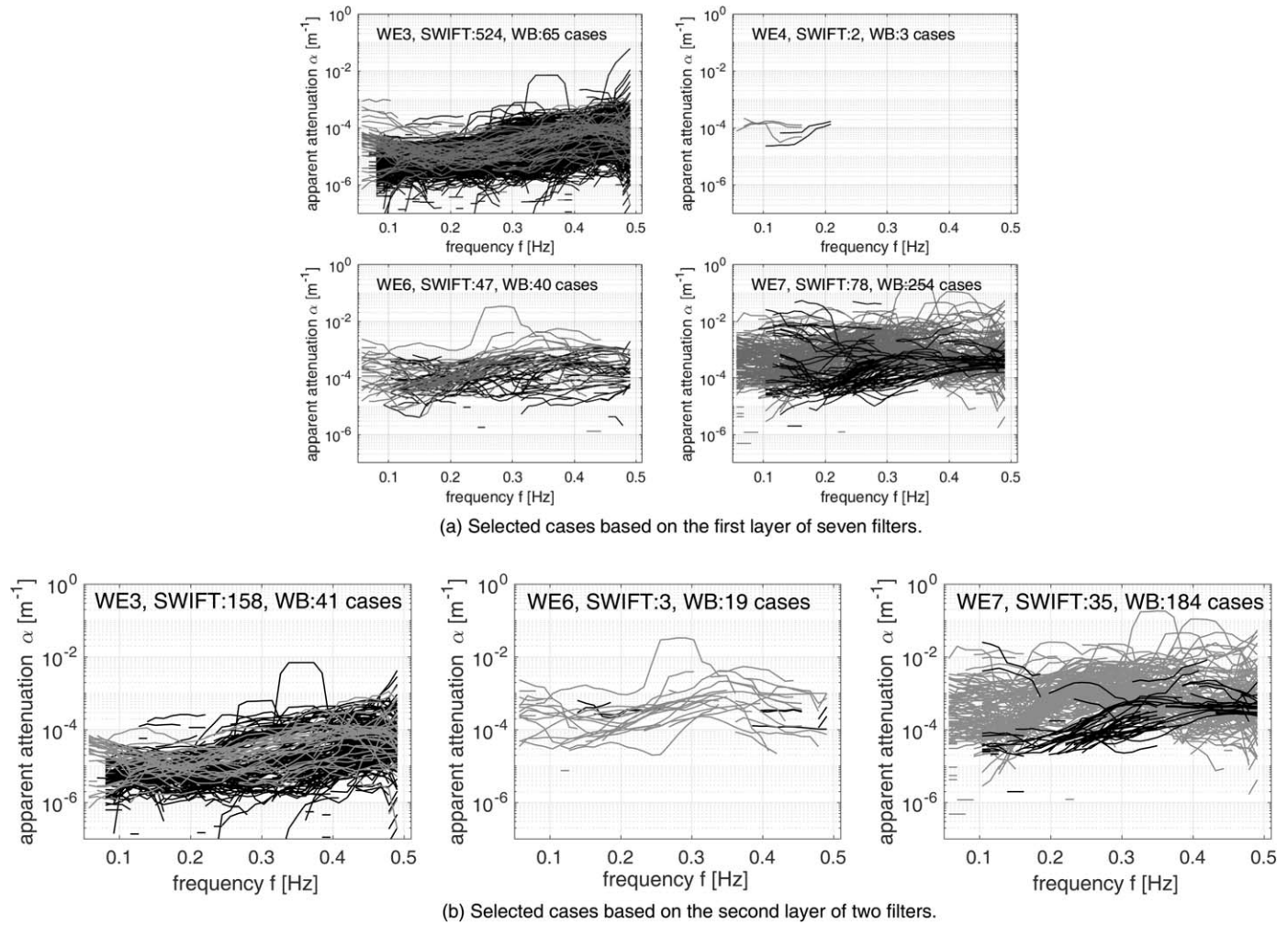
**Figure 4.** Collection of the apparent attenuation coefficient $\alpha$ in WE3, 4, 6, 7 based, (black – SWIFT, grey – WB. (a) Selected cases based on the first layer of seven filters. (b) Selected cases based on the second layer of two filters.

To investigate if those curves may cluster into different groups due to some underlying causes, we apply a pattern recognition method (Huang, 1998) to the $\alpha$ curves. The MATLAB *kmeans* function based on the k-means clustering algorithm (Hartigan, 1975) is employed to perform this clustering. This algorithm uses relative distance between objects to determine if they belong to the same cluster. For the present case, the distance between two curves, $\alpha_1$ and $\alpha_2$, is defined as the sum of distances, i.e., $\Sigma_j|\alpha_{1,j}-\alpha_{2,j}|$. The number of clusters in *kmeans* function is preset at 1/20 of the total number of cases in WE3 and WE7 shown in Figure 4b. For WE6, because of the small number of cases, we do not perform further clustering. After sorting cluster members in descending order, the top three clusters are selected for model calibration in section 5. Other clusters with few members are ignored. Figure 5 shows selected $\alpha$ curves colored in blue, green and magenta, respectively, in descending order of their sizes. The values of $\alpha$ in WE3 are commonly lower than that in WE6 and 7. In WE7, many cases show rollover (existence of a peak) of the apparent attenuation $\alpha$ between 0.3 and 0.4 Hz. As we will discuss subsequently, the rollover is not physical, but is rather an apparent signal related to other source terms.

## 5. Calibration

In this section, we calibrate the parameters of the viscoelastic model using the selected cases in WE3, 6 and 7 (Figure 4b). The parameters are the effective shear modulus $G$ and effective viscosity $v$. Two methods are
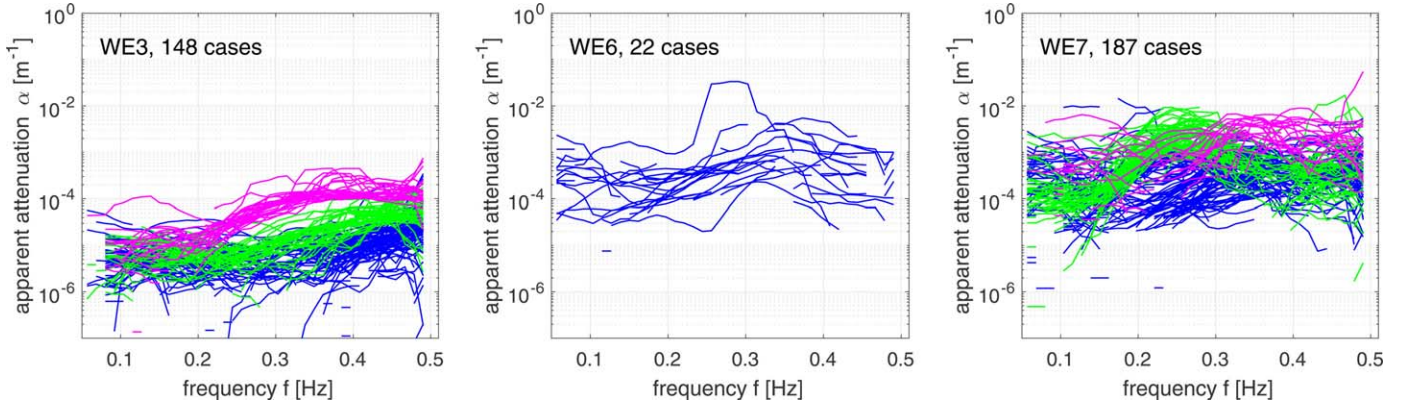
**Figure 5.** Selected cases for calibration through k-means clustering method with ice sources from AMSR2 + SMOS.

adopted. Assuming steady state wave and ice conditions for the 30-min time span in each buoy record, $\frac{\partial F}{\partial t}$ in equation (2) disappears, and all coefficients in equation (2) are constant. Therefore,

$$c_g \frac{\partial F}{\partial x} = (1-C)(S_{in}+S_{ds})+S_{nl}+CS_{ice} \qquad (6)$$

As mentioned in section 3, the simple method regards ice as the only attenuation source, while the full method includes all four sources in equation (2). The calibration is carried out by solving a two-objective optimization problem. In both methods, two objective functions are defined in terms of $k_r$ and the apparent attenuation $\alpha$, respectively. We assume that in all cases studied here, $k_r \approx k_{ow}$, as shown in Figure 2. Hence one objective function is to minimize the difference between $k_r$ and $k_{ow}$. The other objective function is based on minimizing the difference between the measured and calculated attenuation. In addition, we impose a constraint for $k_r$ as $|\frac{k_r}{k_{ow}} - 1| < 0.4$ based on the observations of $k_r$ shown in Figure 2. Pairs of $(G, v)$ are obtained using the Multi-Objective Genetic Algorithm (MOGA) (Murata & Ishibuchi, 1995).

### 5.1. Simple Method
In the simple method, we consider the ice effect $S_{ice}$ as the only attenuation source. Therefore, equation (6) is simplified to

$$c_g \frac{\partial F}{\partial x} = CS_{ice} \qquad (7)$$

In equation (7), $S_{ice}$ is the temporal decay rate of wave energy per unit surface area assuming fully ice-covered. Using the exponential decay of the wave amplitude $A$ defined by the imaginary part of the wavenumber $k_i$ in equation (4), we have $A(x)=A(0)e^{-k_i x}$. In terms of the energy spectral component, $F(f, \theta)$, the spatial energy decay is $2k_i F$ if fully ice-covered. From the assumption $\alpha=Ck_i$ and equation (7), we have

$$\frac{\partial F(f, \theta)}{\partial x} = -2\alpha(f)F(f, \theta) = -2Ck_i(f, G, v)F(f, \theta) \qquad (8)$$

In this study, $\theta$ is the mean direction calculated using measured directional moments at frequency $f$ (Kuik et al., 1988). The effective shear modulus $G$ and effective kinematic viscosity $v$ need to be calibrated so that the measured and calculated wavenumbers across the frequency space match. Two objective functions concerning the attenuation coefficient $\alpha$ and the wavenumber $k$ over the whole frequency domain $f$ are:

$$\mathcal{F}_1 = \min_{G, v} \|k_{ow}-k_r\|_2 \qquad (9a)$$

$$\mathcal{F}_2 = \min_{G, v} \|w(\alpha-Ck_i)\|_2 \qquad (9b)$$

where $\alpha$ is the apparent attenuation; $k_r$, $k_i$ are real and imaginary part of the wavenumber solved from equation (4), respectively; $w$ is the weighting factor: $w(f)=S(f)f^4$.

In $\mathcal{F}_2$, the weighting factor $w$ affects the optimization results. For instance, if $w=1$, the optimization is determined mainly by the portion of the $\alpha$-curve that has the greatest values, usually found at some high frequencies. If $w=S(f)$ then the solution is biased toward the frequency band that contains the most wave energy. Information from other frequency bands is ignored. Note that $\alpha(f)$ spans at least two orders of magnitude in Figure 4, and most of wave energy is between 0.1 to 0.2 Hz based on the measured wave power spectral density (not shown). The weighting factor $w$ proposed above is proportional to the mean square slope of the surface elevation (Rogers et al., 2016).

## 5.2. Full Method

When using the full method, wind input $S_{in}$, wave dissipation $S_{ds}$ and nonlinear wave-wave interaction $S_{nl}$ are added between two buoys.

$$c_g \frac{\partial F(f,\theta)}{\partial x} = -2c_g\alpha F(f,\theta) = (1-C)(S_{in}+S_{ds})+S_{nl}+CS_{ice} \tag{10}$$

The wind input $S_{in}$ and wave dissipation $S_{ds}$ are calculated using formulations from Snyder et al. (1981) and Komen et al. (1984). This choice is called ST1 in the WW3 manual. There are currently five different formulations for $S_{in}+S_{ds}$: ST1, 2, 3, 4 and 6. We choose ST1 because the others require extensive coding to implement. Since our focus is not on studying the wind source and wave breaking, we use the most expedient formulation here. For the nonlinear transfer term, $S_{nl}$, we select the Discrete Interaction Approximation (DIA, Hasselmann et al., 1985). Details of these formulations and associated coefficients are listed in the Appendix A, equations (A6–A9). All of these source terms have been developed for the open sea. They are adopted for lack of studies in partially ice-covered regions.

As in the simple method, there are two objective functions:

$$\mathcal{F}_1 = \min_{G,\nu} \|k_{ow}-k_r\|_2 \tag{11a}$$

$$\mathcal{F}_2 = \min_{G,\nu} \left\| w\left[\alpha - \left(\frac{(1-C)(S_{in}+S_{ds})+S_{nl}+CS_{ice}}{2c_gF(f,\theta)}\right)\right] \right\|_2 \tag{11b}$$

where $w$ is the same as that in equation (9b). Note that the three terms $S_{in}$, $S_{ds}$ and $S_{nl}$, are time rate of change of the local energy. To compute $S_{in}$, $S_{ds}$ and $S_{nl}$ over a distance between two buoys sometimes with large separations, these gain and loss terms need to be integrated over smaller spatial increments. For example, the distance between a pair of buoys varies from 1 to 90 km in WE3. Using the mean wind and ice conditions between the two buoys thus may not be justified. Therefore, we discretize the distance into $n$ equal intervals with size $\leq 2$ km. Then, for each source term $S_I$, we calculate $S_{Isub}$ in each interval. The total value $S_I$ is equal to the sum of $S_{Isub}$ at all intervals.

## 5.3. Calibration Results

For each case shown in Figure 5, through the simple method or the full method, a pair of $(G,\nu)$ is optimized using the Multi-Objective Genetic Algorithm (MOGA). MOGA is realized using function *gamultiobj* in the MATLAB Optimization Toolbox. In this two-objective function problem, there is commonly no solution that can simultaneously optimize both objective functions at the same time. Alternatively, MOGA gives a series of optimal solutions. The connecting curve of these solutions is called Pareto front. At the Pareto front, the two objective functions can no longer be improved simultaneously. In this paper, since solutions on the Pareto front all satisfy the constraint imposed on the real part of wavenumber, we thus choose a solution corresponding to the minimum of equation (9b) for the simple method or equation (11b) for the full method.

A search domain for $G$ and $\nu$ needs to be specified to start MOGA. Furthermore, initial guesses need to be populated in this domain. The domain of $(G,\nu)$ is selected to be from 0 to $10^7$ Pa for $G$ and from $10^{-4}$ to $10^3$ m$^2$/s for $\nu$. This domain covers all values suggested in the existing literature that models grease/pancake ice as an elastic, viscous, or viscoelastic material (e.g., Doble et al., 2015, Newyear & Martin, 1999; Rabault et al., 2017; Zhao & Shen, 2015). The initial guesses are created by a uniform distribution over the entire domain of $(\log_{10} G, \log_{10} \nu)$. It is important to use the log scale to populate the initial guess, because of the very large scale of the parameter space. To use the log scale, the lower limit for $G$ is moved from 0 to
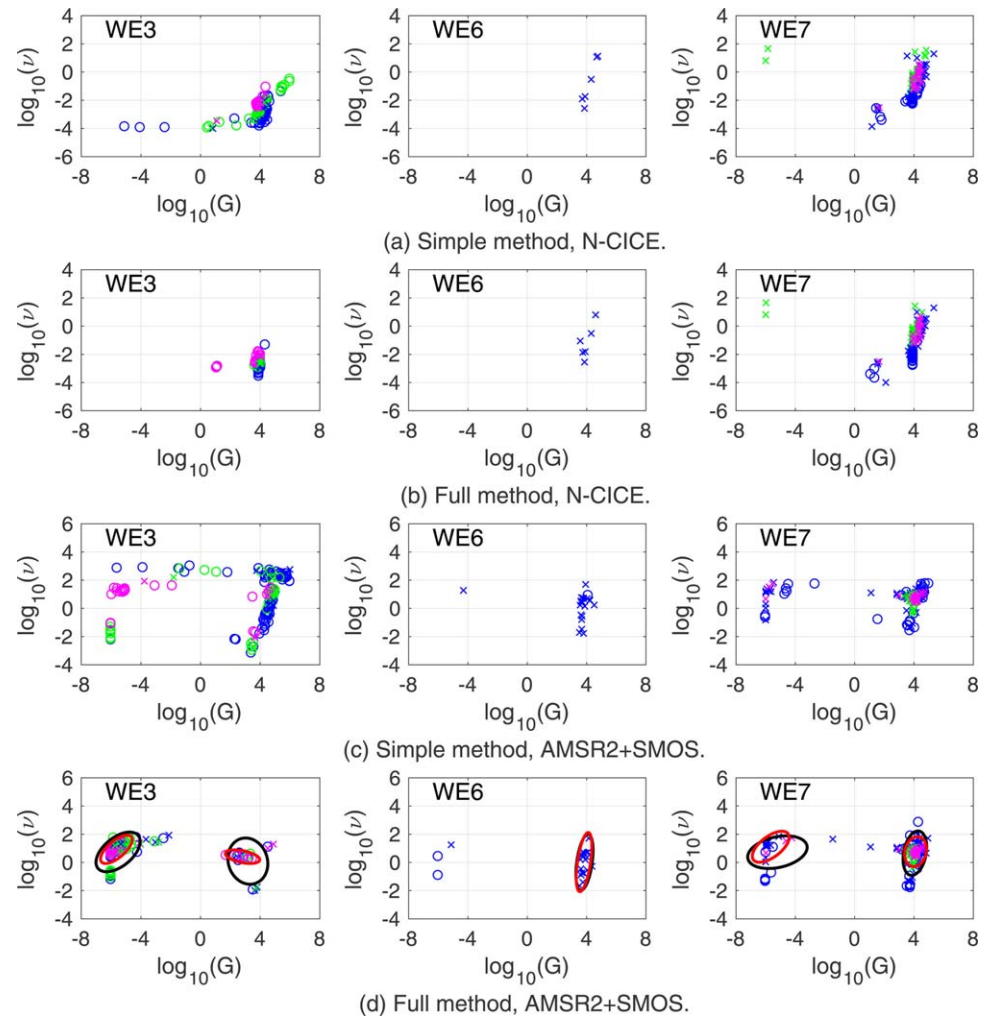
**Figure 6.** Scatter plots of calibrated $(G, v)$ from the full method with ice data from N-CICE and AMSR2 + SMOS. Colors of clusters are consistent with Figure 5. Circle and cross symbols represent data from SWIFT and WB buoys, respectively, in Figure 4b. (a) Simple method, N-CICE. (b) Full method, N-CICE. (c) Simple method, AMSR2+SMOS. (d) Full method, AMSR2+SMOS.

$10^{-7}$ Pa. At such low value, $k$ is insensitive to variations of $G$. An example of the optimized solution in an individual case is given in the supporting information Figure S14.

Figure 6 shows the resulting points of the optimum $(G, v)$ from combining two different ice products and two different solution methods. From each combination, there are three panels, representing results for WE3, 6 and 7, respectively. Each $(G, v)$ point is associated with one of the curves in Figure 5 with the same color. The values of $(G, v)$ span several orders of magnitude, hence they are presented in the log-log scale plots. Results shown in part (d) are most relevant. It uses the full method that accounts for source/sink terms beyond just $S_{ice}$, and uses the more accurate ice product. Parts (a-c) are included for comparison.

The calibration results depend highly on the solution method used and the ice product. Between the two methods, simple and full, we observe larger differences of the resulting $(G, v)$ in WE3, because the wind condition was on-ice, nearly parallel to the peak wave direction, and strong. In WE6 and 7, such conditions were absent, and wind speed was lower (supporting information Figures S5 and S11), but ice conditions were heavier than those in WE3 (Table 2). The two ice products, N-CICE and AMSR2 + SMOS do not always agree as to whether ice is present. A region marked in ice from AMSR2 + SMOS sometimes is marked as open water from N-CICE. Therefore, a portion of the cases indicated as in partial ice cover from AMSR2 + SMOS, are further removed from the calibration when using the N-CICE products for calibration. The

**Table 3**
*Parameters of Bivariate Normal Distributions of the Calibrated $(G, v)$ Using the Full Method*

| WE No. | $\mu_X$ | $\mu_Y$ | $\sigma_X^2$ | $\rho\sigma_X\sigma_Y$ | $\sigma_Y^2$ |
|---|---|---|---|---|---|
| 3 | −5.65 | 0.93 | 0.17 | 0.11 | 0.15 |
|   | 2.82 | 0.41 | 0.17 | −0.03 | 0.03 |
| 6 | 3.83 | 0.03 | 0.04 | 0.10 | 0.72 |
| 7 | −5.66 | 1.11 | 0.27 | 0.15 | 0.22 |
|   | 4.11 | 0.77 | 0.08 | 0.02 | 0.17 |

*Note*: WE3 and WE7 have two clusters shown in Figure 6, thus two sets of mean and standard deviation. $X = log_{10} G$, $Y = log_{10} v$, $\mu$: mean, $\sigma$: standard deviation, $\rho$: correlation coefficient.

resulting numbers of cases in Figures 6a and 6b are therefore less than in Figures 6c and 6d. When both N-CICE and AMSR2 + SMOS show presence of ice, N-CICE in general has concentration and thickness much higher than AMSR2 + SMOS (supporting information Figures S6, S7). Therefore, to match the apparent attenuation using N-CICE, lower values of $v$ are expected. Henceforth, we focus on the results from the full method, because it considers more complete physics, and from the AMSR2 + SMOS ice products, because they agree better with the ship track observations.

To further study the statistics of the calibrated results in Figure 6d, we note that the scatter plots show that most data points gather into one or two clusters. The k-means method is again used to identify these clusters. For each plot, number of clusters is set to two. We then apply a Bivariate Normal Distribution (BND) to fit all data points belonging to a cluster. A black contour represents values of the Probability Density Function (PDF) of the BND equal to 0.05. Points outside this contour are considered outliers and removed from further analysis. A BND fit is again obtained for the remaining points. The red contour represents the 0.05 probability contour of this second BND. Hence, upon removing the outliers, approximately 95% of $(G, v)$ points in a group fall inside the corresponding red ellipse. After these procedures, the domain bounded by the red contour is defined as the range of calibrated $(G, v)$. Parameters of these second BNDs of Figure 6d are summarized as well as corresponding ice conditions in Table 3, where $\mu$ and $\sigma$ are the mean and standard deviation of the PDF. The subscripts indicate $X = log_{10} G$, $Y = log_{10} v$, and $\rho$ is the correlation between $X, Y$ defined in the covariance matrix. The values obtained here are on a par with laboratory measurements using grease/pancake ice (Zhao & Shen, 2015). Except in WE6, viscosity values in other WE's are higher than pure grease ice (De Carolis & Desiderio, 2002; De Carolis et al., 2005; Newyear & Martin, 1999). Definitions of BND and the covariance matrix are given in the Appendix A. The range described by these values will be validated in the next section.

We note that the range of $G$ is lower in WE3 than WE6 or 7. From Table 2, except in WE4, there was virtually no thick ice (second, multiyear, or fast ice) present in these cases. WE3 was strictly a mixture of pancake and thin ice. WE7 had a large share of other types of ice (grey, first year, and brash ice). We note that while in the ASSIST protocol there was no distinction among pancake ice, visual observations showed a wide range of different sizes at different locations and time, formed from composites of smaller pancakes. Detailed analysis of floe size distribution will rely on data collected from different imaging systems. These analyses are underway by several participants of this field campaign.

Figure 6 also shows that from the same cluster of the $\alpha$ curves, the resulting $(G, v)$ are scattered. As mentioned earlier, $\alpha$ is the product of all source terms, while $(G, v)$ is characterized by the ice cover only. Variability in external forcing, particularly the wind, can produce very different apparent attenuation $\alpha$ even with the same ice cover and thus $k_i$. In Figure 6 the $(G, v)$ points form different clusters. In terms of $G$, WE3 and 7 have two clusters each. The majority of points in WE3 are in a cluster with small $G$, while the situation is reversed in WE7. For WE6 in the middle panel of Figure 6d, there is only one cluster identified because there are too few points in the second cluster for $G < 10^{-4}$ Pa. We will return to this point in section 7.

## 6. Validation

In this section, we use two independent datasets to validate the calibrated parameters. One dataset is from the selected cases in WE4, the other dataset is from two wave sensors that were operational in WE3 but not used in the calibration; one of them is the NIWA buoy and the other is a moored acoustic wave and current profiler (AWAC). Their locations, which are far from the main array of buoys in WE3, are indicated in supporting information Figure S10.

### 6.1. Validation With Wave Experiment 4
The first validation test compares model results using the calibrated values of $(G, v)$ based on WE3, 6, and 7, and the wind and ice conditions for each WE4 buoy pair to calculate apparent attenuations $\alpha$. The wind conditions during WE4 were marked by fairly short period of weak on-ice winds and predominant, though also
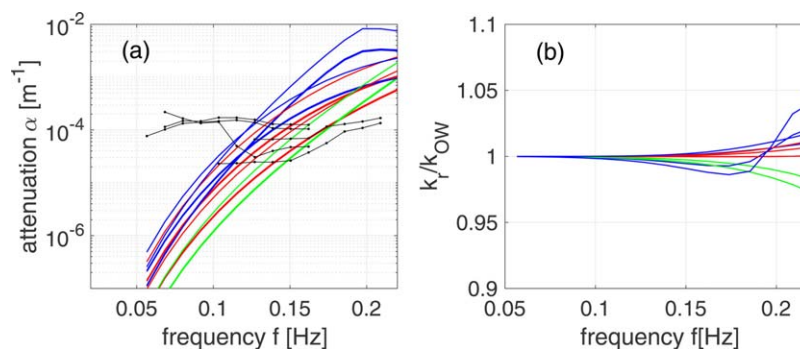
**Figure 7.** Validation results of $(G, \nu)$ with cases from WE4 (shown in Figure 5(a)); (a) comparison of apparent attenuation $\alpha$; black curves are measure values repeated from Figure 4(a), colored are model results using the mean $(G, \nu)$ from Table 3: red-WE3, green-WE6, blue-WE7; (b) corresponding ratio of modeled $k_r$ over $k_{ow}$.

weak, off-ice winds (supporting information Figure S5). The ice condition in WE4 was different from the other WE's in that thick ice was present (Table 2 and supporting information Figure S8). In WE4, the wave amplitude was low, with no reliable apparent attenuation data at high frequencies (Figure 4a). This was the reason that WE4 was rejected in the second filtering process for calibration.

As mentioned in the previous section, we validate only the results from the full method, and the AMSR2 + SMOS ice products. We select the center pair(s) $(G, \nu)$, i.e., $10^{\mu_X}$ and $10^{\mu_Y}$ from Table 2, from each of the calibrated elliptical ranges for each of WE3, 6, 7. By substituting them into equations (4) and (10), we may solve the selected cases in WE4 for $\alpha$ and $k_r$. Comparison of the modeled (colored) and the measured $\alpha$ (black) are shown in Figure 7a. The modeled $k_r$ is shown in Figure 7b, but there is no measured data to compare with. Based on the ice morphology shown in Table 2, we expect that WE6 and 7 should match WE4 better than WE3. The results in Figure 7a appear to confirm this speculation. Despite the differences in the ice, wind, and wave conditions, the calibrated values from WE3, 6, and 7 are able to capture the magnitude of attenuation observed in WE4. By including a broader range of $(G, \nu)$, for instance, from the red ellipses in Figure 6, nearly all black curves are bounded within the calibrated theoretical results. (Not shown here.) It is apparent that the curves from measured data are all flatter than the model results. This phenomenon persists even when applying a broader range of $(G, \nu)$. Low signal strength due to weak wave energy in WE4 cannot fully explain this discrepancy. Lower damping from model results for long waves is also observed in WE3 as shown in the next section.

### 6.2. Validation With NIWA Buoy and AWAC Mooring in Wave Experiment 3

The second validation compares a WW3 hindcast run covering the Beaufort Sea for the period of WE3 with two additional wave measurements not used in calibration. The ice source term follows IC3, the viscoelastic model, with $(G, \nu)$ chosen from the calibrated range of WE3. As mentioned earlier, WW3 has five switches, ST1–4 and ST6, for calculating wind input and wave breaking dissipation terms together. We use ST1 to execute the simulation, for consistency with the calibration. The rest of this hindcast design follows what was described in Rogers et al. (2016).

The resulting simulated wave field is co-located and compared with the wave data from the NIWA buoy and an AWAC mooring. Relative to the center location of WE3 in Table 1, the NIWA buoy was nearly 130 km away to the north-west, and the AWAC, moored at (75°N, 150°W), was about 230 km away to the north (supporting information Figure S10). The ice type at the NIWA site was believed to be similar to the rest of the buoy sites in WE3, as verified by a photo taken at its retrieval. There was no visual information of the ice condition at the AWAC site. We use the cluster of $(G, \nu)$ with the lower values of $G$ from Figure 6d in the WE3 case for this validation, because this cluster contains the majority of cases selected in WE3.

The model and observation results are compared in Figure 8. For the AWAC comparison. Hourly AWAC observations of the significant wave height $H_s$ and $T = \dfrac{\int_{f_1}^{f_2} E(f)^4 df}{\int_{f_1}^{f_2} E(f)^4 f df}$ (Young, 1995), a peak wave period surrogate, are shown for the duration of WE3. This $T$ has the advantage of being smooth and closely approximates the peak wave period. Modeled $H_s$ and $T$ at the location of the AWAC compare well with the
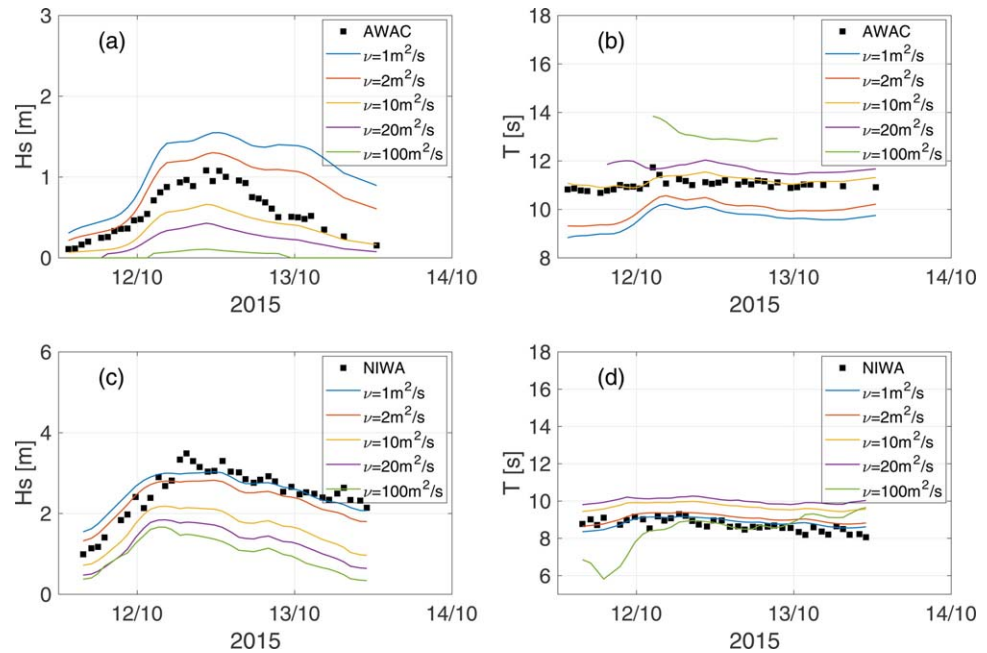
**Figure 8.** Comparison of the model and observed wave height and period at (a,b) the AWAC and (c,d) the NIWA sites. The model results are obtained by running WW3 with elastic coefficient $G=0$ Pa for all cases, and viscous coefficient $v=1$, 2, 10, 20, 100 m$^2$/s (blue, red, yellow, purple, and green lines, respectively).

observations, with viscous coefficient $2 < v < 10$ m$^2$/s appearing most appropriate for both. For the same set of parameters tested, the agreement between the modeled and observed $H_s$ and $T$ from the NIWA buoy is less satisfactory. For both cases, since the ice condition in WE3 was changing fast, using any constant $(G, v)$ values for the entire duration of WE3 may not be appropriate.

## 7. Discussion

### 7.1. Assumptions Made in the Radiative Transport Equation

This study is based on the radiative transport equation, equation (2). We assume that the time rate change is much smaller than the convective transport term, hence $\partial F / \partial t$ is ignored in equation (6). In rapidly changing wave field such as WE3, this term could be of equal or more importance as the convective term. While detailed analysis of the relative importance of these two terms requires further study, we may estimate the effect of including the time derivative as follows. Moving $\partial F / \partial t$ to the right hand side of equation (2), it becomes an effective source/sink term. In a rising wave field, $-\partial F / \partial t$ is an additional sink term. It increases the apparent attenuation coefficient $\alpha$, and the resulting $k_i$. In a falling wave field the opposite happens. However, even if we double or halve the $S_{ice}$ term in equation (2), against the already broad range of $\alpha$ shown in Figure 5, its effect on the range of $(G, v)$ is minor. We thus accept the present results.

### 7.2. Comparisons With Rogers et al. (2016)

Rogers et al. (2016) studied WE3 extensively. They separated the wave data into different ice types to investigate the relationship between the attenuation rate $k_i$ and wave frequency $f$. A different inverse method from the present study was employed to obtain $k_i$. Instead of determining the attenuation from pairs of buoys as is done in the present study, the authors determined $k_i$ inversely from WW3 simulations of the Beaufort Sea, covering the region of WE3. WW3 was run with a variety of $k_i$ using switch IC1 for $S_{ice}$, and ice data from N-CICE. Choosing $k_i$ for each frequency $f$ that corresponded to the best match of the power spectra density at the given frequency between the WW3 result and the buoy measurement, the calibrated $k_i - f$ curve was determined for each record from the SWIFT buoys. Ice type (and thickness) was identified to be the natural grouping factor, because source terms in addition to the ice cover were already included in the WW3 analysis. Within the six types of surface conditions classified using the SWIFT camera images, there was a natural ranking of the attenuation coefficient $k_i$.
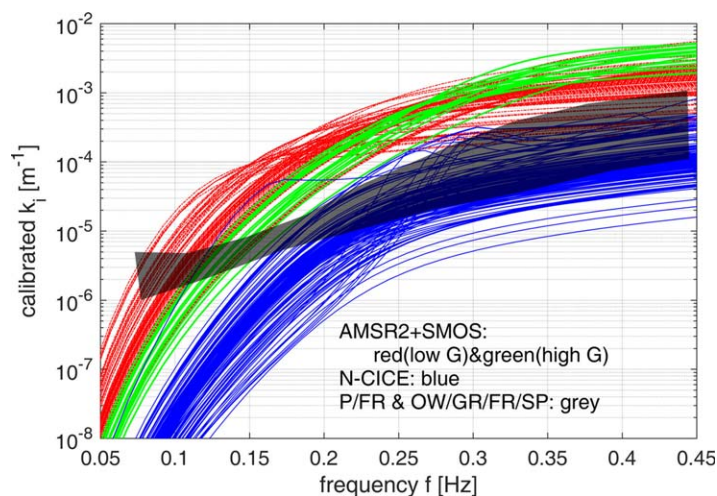
**Figure 9.** Comparison of attenuation rate $k_i$ obtained in WE3 between calibrated results (red, green, and blue curves) and Rogers et al. (2016) (black bands). In the calibrated results, two ice products are used. When AMSR2 + SMOS are used, $(G, v)$ are from the two ellipses shown in Figure 6(d), one corresponding to low $G$ (red) and the other with high $G$ (green). When N-CICE is used, all curves are shown in blue. Partial results from Rogers et al. (2016) Figure 8 are shown, representing the majority of cases classified in that paper as pancake/frazil ice or open water/grease ice/frazil ice/sparse floes type.

Figure 9 shows a comparison between the $k_i - f$ curves from the present study and Figure 8 of Rogers et al. (2016). In this work, $k_i$ curves of the selected cases are obtained through equation (4a) with the calibrated $(G, v)$ from the full method. Results from using the N-CICE and AMSR2 + SMOS products are both examined. All cases shown are from WE3. The red and green curves are from the calibrated $(G, v)$ with AMSR2 + SMOS ice products, shown in the red ellipse in Figure 6d, with the red corresponding to the cluster with lower $G$ and green to the higher $G$. The blue curves correspond to calibration results using ice products N-CICE shown in Figure 6b. From Rogers et al. (2016), we include only two types of ice covers: pancake in frazil (P/FR) and sparse pancakes or pancake debris (brash) in either i) mixed open water and frazil, or ii) frazil (OW/GR/FR/SP). Other types are excluded in the present study due to the ice concentration and thickness filters applied prior to the data analysis.

Comparing with Rogers et al. (2016), $k_i$ associated with AMSR2 + S-MOS are greater except at the very low frequency end. As shown in supporting information Figure S6 and S7, values of ice concentration from N-CICE are usually much larger than from AMSR2. Therefore, when using AMSR2, to make up for the lower ice thickness and concentration, a greater $k_i$ is expected. At the low frequency end, the viscoelastic model under-predicts the measured attenuation as demonstrated in Rogers et al. (2016).

Comparing the two studies both with N-CICE, we note that the blue curves from the present $k_i$ values are generally smaller than those from Rogers et al. (2016). There are several possible effects that may contribute to this discrepancy. In Rogers et al. (2016), the $k_i(f)$ is calculated for each buoy spectrum, independent of other buoy spectra; thus the $k_i(f)$ is representative of the dissipation by ice between the open water (to the southeast) and the buoy. In the present study, $k_i(f)$ is calculated from buoys pairs, so $k_i(f)$ is representative of the dissipation by ice between the two buoys. The treatment of open water physics in Rogers et al. (2016) and the present study is also different. The former used the ST4 source term package and the present uses ST1. In addition, in the present study we ignore the $\partial F/\partial t$ term in equation (2) as mentioned above. This term may be comparable to the spatial derivative term especially in rapidly changing wave field such as WE3. In Rogers et al. (2016), this term is automatically included when using WW3. With these differences, we do not expect a perfect agreement between the Rogers et al. (2016) results and the present one, even when both used N-CICE for ice data source.

Regarding the ice cover variations in the study region, apparently at different time (and location) the characteristics of ice cover changed significantly, as the photos in Figure 3 show. Even at the same time within the distance between two buoys the ice cover was not homogenous. Hourly ASSIST-protocol observations of ice during the wave experiments typically reported multiple ice types within the field of view of the SKQ. One example of this situation is shown in Figure 10 obtained from MR on SKQ during WE3. Two buoys are in view in Figure 10a. The color bar in Figure 10b represents the intensity of the radar backscatter of the surface around the ship, which is an indication of the ice type or thickness. The inhomogeneity at this scale is evident.

### 7.3. Factors Behind the Clustering of the Apparent Attenuation

The apparent attenuation curves for each WE shown in Figures 4 and 5 are wide spread. In Rogers et al. (2016), where only WE3 data were used, similar spread was found. In the present study, these apparent attenuation curves are results of all source/sink terms as mentioned earlier. We used k-means method, a common pattern recognition method to detect clustering of these curves and included the top three most populated clusters in Figure 5 for the calibration work. We now investigate the causes for this clustering phenomenon.

Time series of buoy locations, wind, and ice conditions for WE3, 4, 6, and 7 are given in the supporting information Figures S1, S2b, and S11–S13. WE6 has relatively few cases to perform a meaningful clustering; hence it is excluded from this discussion.
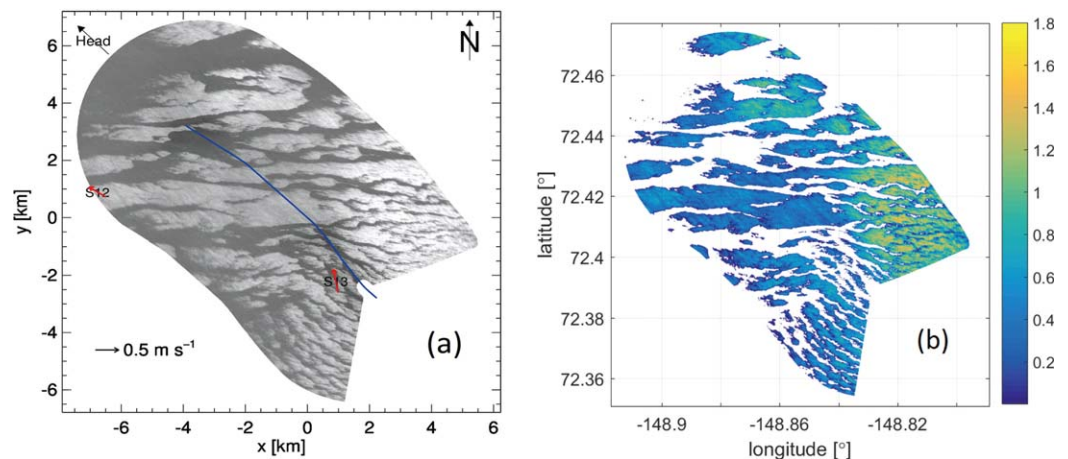
**Figure 10.** A marine radar image taken during 11 October 2015 15:08–15:42. (a) km scale (b) longitude-latitude scale. The origin of Figure 10a is at (72.41°, −148.85°). The blue curve is the ship track over the time period (∼30-min) of this image. Bright is ice, dark is water or grease ice. Two SWIFT buoys, S12 and S13, were in the vicinity of the ship track. The red arrows mark their drift directions. In Figure 10b, the color bar represents the backscatter strength relating to the ice type.

WE3 was during a strong wave event with on-ice wind and wave directions. In general, the magenta curves in Figure 5a are above the green and blue ones. The latter two have significant overlap. Most of the magenta curves correspond to the later part of WE3 (13 October 2015), when wind from the NAVGEM data-set shows decrease from 15–17 m/s to 11–13 m/s. As the energy input from wind is smaller, the apparent attenuation of the magenta cluster is higher than those of the other two clusters. Between the blue and green clusters there was no significant difference in wind speed, ice concentration, ice thickness, buoy locations or distance between buoys.

Buoys deployed in WE7 were much closer together than in WE3. Except a zigzag initially displayed by some buoys in response to the shifting wind direction, they drifted nearly in the same direction during the entire time (supporting information Figure S1). Hence, the separation in each buoy pair used in the analysis was much smaller than those in WE3 (supporting information Figure S2). We thus expect that the ice and wind conditions between the buoys were much more uniform. The floe size was significantly greater than what was found in WE3 as shown in Table 2 and Figure 3. In the beginning of WE7, all buoys were close to each other, and most of the curves belong to the blue cluster. As the buoys drifted apart from 1 November 2015, most of the green curves were from buoy pairs farther away from the ice edge, corresponding to higher attenuation and most of the blue ones were from pairs near the ice edge, resulting in lower attenuation. Many curves (mainly from the green cluster) demonstrated a rollover. It is expected that wind input and nonlinear energy transfer between frequencies can produce a rollover in the apparent attenuation, but these effects should only become significant when the distance between buoys are large and the wind is strong. Why such rollover was only observed in WE7 and less so in WE3, with the latter having more favor-able conditions for rollover, is puzzling. It is important to note that this rollover is in the *apparent* attenuation $\alpha$, not the actual attenuation $k_i$ shown in Figure 9.

### 7.4. Relation Between Attenuation and Ice Morphology

Figure 6d shows in WE3 and WE7 there are two clusters of $(G, v)$. The resulting $k_i$ curves as shown in Figure 9 are similar except between 0.1 and 0.15 Hz. We investigated the objective function $\mathcal{F}_2$ and found that there were several local minima. Details of $\alpha$ curves determine which of the local minima gives the global optimum solution of $(G, v)$. Parameters $k_i$ and $(G, v)$ are directly related to the $S_{ice}$ term associated with the ice type, while $\alpha$ shown in Figure 5 is a result of all other source terms $S_{in}$, $S_{ds}$ and $S_{nl}$. The clusters in Figure 5 become mixed in Figure 6 and Figure 9. Further classification using the ice types as shown in Rogers et al. (2016) may separate the $k_i$ and $(G, v)$ results into different clusters. This idea was tested. Each $k_i$ curve was associated with an ice code defined by the type of ice encountered, whenever an image from the SWIFT camera was available. The result did not show clear correlation between $k_i$ and the ice type, probably due to the fact that ice covers were inhomogeneous between buoys that were far apart, as indicated in Figure

10. Ice type classification over the scale of buoy distance is needed to better correlate ice types with the $k_i$ behavior. Nevertheless, a general observation may be made from Table 2, which shows that the ice morphology does differ in the four WEs. With WE3 being the only one lacking thicker ice, the resulting $(G, v)$ shown in Figure 6d are mostly clustered near $G \sim 0$, while WE6 and WE7 cluster more near $G \sim 10^4$ Pa.

However, one caveat has to be kept in mind: in this study, wind input $S_{in}$ and ice damping $S_{ice}$ are usually of the same order of magnitude and both terms are much larger than $S_{ds}$ and $S_{nl}$. Hence, the wind models in WW3 manual (Tolman & the WAVEWATCH III® Development Group, 2016) may significantly change the calibration results for ice attenuation. If the wind input were lower, the apparent ice attenuation would be greater.

### 7.5. Uncertainties in the Calibration Method

The main goal of the present study is to use the SeaState data to calibrate $(G, v)$ for the viscoelastic model with an optimization procedure. The objective functions of this optimization include matching the real and the imaginary components of the complex wavenumber. Data for the real part of the wavenumber are very limited. From the results obtained with two independent methods from WE3 in Figure 2, one consistently shows shortening of waves through the pancake ice cover and the other shows both lengthening and shortening. In either case, deviation from the open water wavelength is small. Hence, $k_r = k_{ow}$ is selected as one of the objective function, $\mathcal{F}_1$, with a constraint for $k_r / k_{ow}$. This objective function may change with future wavelength data.

The imaginary part of the wavenumber is related to the apparent attenuation $\alpha$, as well as wave and wind field, ice concentration and thickness. The accuracy of the measured $\alpha$ is associated with the wave energy level. At very high or low frequency bands, data for the directional wave spectra are less reliable. We removed this uncertainty by eliminating data with low energy (see the 7 basic filters in section 3). But still, with the remaining data, we find that the wave direction varied significantly between adjacent frequency bands. The wave direction directly affects the $\alpha(f)$ in equation (5) through the projected distance $D_{AB}$. Although intuitively we expect a smooth variation of wave directions between frequency bands, no modification is attempted in the present study to remove this strong directional variability.

The other important factor in this second objective function, $\mathcal{F}_2$, is the weighting factor $w$ shown in equations (9b) and (11b). After trying many cases, we identify two that are most physically meaningful. One sets $w(f) = S(f) = \int_\theta F(f, \theta) d\theta$ and the other sets $w(f) = S(f) f^4$. The first tries to match the significant wave height, the second tries to match the spectral moment $m_4$. Figure 6 presents results from the second weighting factor. Results of $(G, v)$ from the first weighting factor are given in supporting information Figure S15. Focusing on the full method with AMSR2 + SMOS, for WE3 we can see the major differences are that with $S(f)$ as the weighting factor, $(G, v)$ are more clustered at larger $G$ and the mean values of both $G$ and $v$ in this cluster are higher than using $S(f) f^4$ as the weighting factor. For WE6 and 7, only minor differences are noted between results from these two weighting factors. Further investigation is required to explain this observation.

### 7.6. Uncertainties in the Input Data Set

Both ice concentration and thickness are part of the radiative transport equation, equation (2). They affect the calibrated $(G, v)$. Only two of many choices for the ice data are presented in Figure 4: N-CICE, which provides both concentration and thickness, and AMSR2 + SMOS, which provides concentration and thickness, respectively. In general, for a fixed set of measured apparent attenuation $\alpha$, higher concentration and thickness produce lower values of $(G, v)$. AMSR2 for ice concentration and SMOS for ice thickness compare well with in-situ observations along the ship track, as shown in supporting information Figures S6 and S7. Therefore they are favored in the present study. Further validation of these various ice data needs to be done.

Likewise, wind data may also be obtained from various sources. We used only those from NAVGEM, based on the agreement between co-located wind data from NAVGEM and SKQ anemometers (see supporting information Figure S9) and SWIFT wind for reference. At present no thorough comparison between different wind sources has been carried out. Under low wind conditions, $S_{in}$ is low compared to $S_{ice}$, the importance of $S_{in}$ over the partially ice covered area increases significantly under high wind (Li et al., 2015).

### 7.7. Issues in the WW3 Model

The radiative transport equation used in WW3 considers many other processes in addition to the ice source term. However, except a $(1-C)$ scaling for $S_{in}$ and $S_{ds}$, there are no modifications made to other terms for a partially or fully ice covered region. No modifications were made to the nonlinear transfer term $S_{nl}$. Questions have been raised in Rogers et al. (2016) concerning these assumptions. Furthermore, in a study concurrent with the present work, Smith et al. (2016) used the ADCP (acoustic Doppler current profiler) on the SWIFT buoys to measure the turbulent dissipation under the ice cover for WE3. They found that the turbulent dissipation under ice cover was distinctly different from the open water cases. The level of the dissipation was found to be generally less than the open water cases, but not negligible. This is consistent with Zippel and Thomson (2016). A more detailed analysis of their turbulence data has been prepared in a separate study for this special issue. Direct measurement of turbulence under ice covers during a wave event in the Barents and Greenland Sea also revealed eddy viscosity values two orders of magnitude greater than that of water (Marchenko et al., 2017). Theories for wave damping due to eddy viscosity were developed by assuming a highly viscous ice sheet (Weber, 1987) or a pure elastic ice sheet (Liu & Mollo-Christensen, 1988). At present, WW3 does provide the option, module IC2, for $S_{ice}$ parameterization to consider eddy viscosity alone. It has not been integrated with module IC3, which considers the attenuation due to the ice cover itself. Additional damping mechanisms, such as porous media flow through brine channels, have also been proposed for solid ice covers (Marchenko & Cole, 2017). Since the apparent attenuation includes all possible source/sink terms in nature, fitting the data to any wave-in-ice model would need to be revisited if other sink term is included in the modeling.

## 8. Final Remarks and Recommendations

### 8.1. Remarks

The study presented here uses many datasets from a broad range of instruments and multiple combinations of analysis. Instead of repeating the long list of findings discussed above, we outline what has been accomplished.

In this study, we fulfill the need to complete a calibration of a viscoelastic ice model included in the global wave model WAVEWATCH III® (WW3). This viscoelastic model synthesized all previously presented continuum models for an ice cover. Two viscoelastic model parameters that characterize the effective elasticity and viscosity of an ice cover are calibrated using field data from the SeaState project. Hundreds of measured attenuation curves with respect to frequencies obtained from three wave experiments were utilized for the calibration. The calibrated viscoelastic model is validated using independent datasets collected in the same field campaign, which show reasonably good agreement with measured wave parameters.

The resulting viscoelastic parameters may be used in WW3 for wave forecasts where pancake ice is dominant, for which the calibration is completed. As pancake ice is widespread throughout the wave-effected Antarctic marginal ice zone, and expected to become more prevalent in the Arctic marginal ice zone, there should be ample opportunities to further validate and refine these parameters. The range of the calibration parameters, $(G, v)$ is large, due to the scatter of the measured data. Based on the validation, we find the method works to constrain the variability present in the field. We believe this scatter can be reduced if careful classification according to ice morphology is employed.

With additional information, the calibrated $(G, v)$ may be fine-tuned to better correlate with different types of ice covers. During the SeaState campaign, there were many observations of ice, winds, and waves that have yet to be investigated. For example, there were five aircraft flights over the region covered by the SKQ track, each including numerous visual, Lidar, and SAR collections. The SWIFT buoys' camera images, continuous video imaging, and pulse stereo-photography from the ship, provide possibilities to obtain high-resolution ice floe size distribution. Many of these datasets are being analyzed concurrently and may further refine the present results.

### 8.2. Recommendations

Ice conditions strongly affect $(G, v)$ values. Hence, wave forecasts are linked to ice forecasts. Current ice models can only provide ice concentration and thickness, some with percentages of different ice thickness categories. But no ice model presently can predict the pancake ice or, for that matter, any other specific types of ice. For short-term forecasts, remote sensing images may be used to detect ice types, provided

that reliable algorithms are developed to identify them. For the present results to be useful in very short-term wave forecasts, pancake ice needs to be located in addition to the thickness and concentration information. Reliable local wind information that includes spatial variability is also important. For long-term forecasts, a dynamic-thermodynamic ice model that can predict the distribution of pancake ice is needed. To apply the viscoelastic model to the entire Arctic Ocean, the current parameterization calibrated exclusively in pancake ice fields is insufficient. A few field experiments in solid pack ice show different wave propagation characteristics (Hunkins, 1962; LeSchack & Haubrich, 1964; Squire et al., 1994). A combination of dedicated field experiments such as in the SeaState project and scaled down laboratory studies are needed to complete the parameterization for all ice types.

## Appendix

1. The Pearson correlation coefficient is

$$r = \frac{\sum_i (x_i - \bar{x})(y_i - \bar{y})}{\sqrt{\sum_i (x_i - \bar{x})^2}\sqrt{\sum_i (y_i - \bar{y})^2}} \tag{A1}$$

where $x_i$ and $y_i$ are the PSD values of the respective buoys at the $i^{th}$ frequency.

2. The "check factor" of a SWIFT buoy is

$$ck(f) = \frac{XX(f) + YY(f)}{ZZ(f)} \tag{A2}$$

where $XX$ and $YY$ are horizontal displacement, and $ZZ$ is vertical displacement (Thomson et al., 2015). The "check factor" of a WB buoy is $\frac{k_r}{k_{ow}}$, where $k_{ow} = \frac{\omega^2}{g}$ is the wavenumber from the open water dispersion relation, and $k_r$ is the estimated wavenumber,

$$k_r(f) = \sqrt{\frac{C_{pitch}(f) + C_{roll}(f)}{C_{heave}(f)}} \tag{A3}$$

where $C_{pitch}$ is the pitch autospectra. $C_{roll}$ is roll autospectra. $C_{heave}$ is the heave autospectra (Kuik et al., 1988).

3. The Bivariate Normal Distribution (BND) probability density function is

$$P(x_1, x_2) = \frac{1}{2\pi\sigma_1\sigma_2\sqrt{1-\rho^2}}\exp\left[-\frac{z}{2(1-\rho^2)}\right] \tag{A4}$$

where $z = \left(\frac{x-\mu_x}{\sigma_x}\right)^2 - 2\rho\left(\frac{x-\mu_x}{\sigma_x}\right)\left(\frac{y-\mu_y}{\sigma_y}\right) + \left(\frac{y-\mu_y}{\sigma_y}\right)^2$, and $\rho = cor(x_1, x_2) = \frac{V_{12}}{\sigma_1\sigma_2}$ is the correlation of $x_1$ and $x_2$ and $V_{12}$ is the covariance. The covariance matrix is defined as

$$V = \begin{pmatrix} \sigma_1^2 & \rho\sigma_1\sigma_2 \\ \rho\sigma_1\sigma_2 & \sigma_2^2 \end{pmatrix} \tag{A5}$$

4. For reproducibility of optimization executed using MATLAB, the random number generation function rng() in MATLAB is set as rng(5). Furthermore, hybrid programming of MATLAB and FORTRAN is used to reduce computational time, where FORTRAN code is used to solve equation (4).

5. In WW3 manual (Tolman & the WAVEWATCH III® Development Group, 2016), when selecting ST1, the wind input term is modeled as

$$S_{in}(f, \theta) = \max\left[0, \ 0.25\frac{\rho_{air}}{\rho_{water}}\left(\frac{u_*}{c}\cos(\theta - \theta_{wind}) - 1\right)\right]\omega F(f, \theta) \tag{A6}$$

$$u_* = u_{10}\sqrt{(0.8 + 0.065u_{10}) \times 10^{-3}} \tag{A7}$$

where $\rho_{air}$ and $\rho_{water}$ are the density of air and water, respectively; $k_r$ is calculated based on the viscoelastic model; $c = \omega/k_r$ is the wave phase velocity; $\theta_{wind}$ is the wind direction; $u_*$ is the wind friction velocity (Charnock, 1955; Wu, 1982); $u_{10}$ is the wind speed at 10 m above the mean sea level. The dissipation term is

$$S_{ds}(f,\theta) = C_{ds}\hat{\omega}\frac{k}{\bar{k}}\left(\frac{\hat{\alpha}}{\hat{\alpha}_{PM}}\right)^2 F(f,\theta) \tag{A8}$$

where $C_{ds}$ is a constant $\left(C_{ds}=-2.36\times10^{-5}\right)$; $\hat{\alpha}_{PM}$ is the value of $\hat{\alpha}$ for a Pierson–Moskowitz spectrum $\left(\hat{\alpha}_{PM}=3.02\times10^{-3}\right)$; $\hat{\omega}=\left(\overline{\omega^{-1}}\right)^{-1}$; $\hat{\alpha}=E\hat{k}^2g^{-2}$, $\hat{k}=\left(\overline{1/\sqrt{k}}\right)^{-2}$. The spectral average of a variable $z$ is defined as $\bar{z}=\frac{\int_0^{2\pi}\int_0^{\infty}zF(f,\theta)dfd\theta}{\int_0^{2\pi}\int_0^{\infty}F(f,\theta)dfd\theta}$. We use the coefficients provided in the WW3 manual in this study. The nonlinear wave-wave interaction term, $S_{nl}$, is calculated using the Discrete Interaction Approximation (DIA, Hasselmann et al., 1985).

$$\begin{pmatrix}\delta S_{nl,1}\\\delta S_{nl,3}\\\delta S_{nl,4}\end{pmatrix}=D\begin{pmatrix}-2\\1\\1\end{pmatrix}C_{nl}g^{-4}f_{r,1}^{11}\left[F_1^2\left(\frac{F_3}{(1+\lambda_{nl})^4}+\frac{F_4}{(1-\lambda_{nl})^4}-\frac{2F_1F_3F_4}{(1-\lambda_{nl}^2)^4}\right)\right] \tag{A9}$$

where $F_i=F(f_i,\theta_i)$ and $\delta S_{nl,i}=\delta S_{nl}(f_i,\theta_i)$, $i=1, 3, 4$. The two constants are: $\lambda_{nl}=0.25$, $C_{nl}=1.0\times10^7$ (Tolman & Chalikov, 1996).

6. The full method in section 4 is explained as follows. We select many cases of pairs from SWIFT and WB buoys to study wave attenuation. The separation between two buoys was sometimes as large as several dozen kilometers. Using the mean values between the two buoys in equations (A6–A9) may be too coarse an approximation. We thus discretize the distance into $n$ equal intervals, where $n$ is the smallest integer for distance/$n < 2$. Then, for each source term $S$, we calculate $S_{sub}$ in each interval, where inputs of equations (A6–A9) are obtained by linear interpolation between the two buoys. The total value $S$ is equal to the sum of $S_{sub}$ at all intervals. For the $m^{th}$ node, the simplified radiative transport equation equation (10) is

$$-2c_g\alpha F_m(f,\theta)=[(1-C)(S_{in}+S_{ds})+S_{nl}]_m+C\left(-2c_gk_iF_m(f,\theta)\right) \tag{A10}$$

where, we assume the attenuation rate $\alpha$ and $k_i$ are constants at all intervals. $F_m=\frac{m}{n}F_A+\frac{n-m}{n}F_B$. Summing equation (A10) at all nodes, it yields,

$$-2c_g\alpha=\frac{\Sigma_m\left[(1-C)(S_{in}+S_{ds})+S_{nl}\right]_m}{\Sigma_m\ F_m(f,\theta)}+C\left(-2c_gk_i\right) \tag{A11}$$

where $\Sigma_m\ F_m(f,\theta)=\Sigma_m\left(\frac{m}{n}F_A+\frac{n-m}{n}F_B\right)=\frac{n+1}{2}(F_A+F_B)$.

## References

Andersson, E. (2015). *User guide to ECMWF forecast products* (129 pp.). Reading, UK: The European Centre for Medium-Range Weather Forecasts.

Charnock, H. (1955). Wind stress on a water surface. *Quarterly Journal of the Royal Meteorological Society*, *81*(350), 639–640. http://doi.org/10.12952/journal.elementa.000095

Cheng, S., Zhao, X., Erick Rogers, W., Thomson, J., & Shen, H. H. (2016). *Preliminary calibration of a rheological sea ice model for wave-in-ice using field data*. Paper presented at 23nd IAHR International Symposium Ice, Ann Arbor, MI, May 31 to June 3.

Collins III, C. O., Lund, B., Ramos, R. J., Drennan, W. M., & Graber, H. C. (2014). Wave measurement intercomparison and platform evaluation during the ITOP (2010) experiment. *Journal of Atmospheric and Oceanic Technology*, *31*(10), 2309–2329.

Collins, C. O., III., & Rogers, W. E. (2017). A source term for wave attenuation by sea ice in WAVEWATCH III® (Tech. Memo. NRL/MR/7320—17–9726). IC4 Naval Research Laboratory.

Collins, C. O., III, Rogers, W. E., & Lund, B. (2017). An investigation into the dispersion of ocean surface waves in sea ice. *Ocean Dynamics*, *67*, 263–280. https://doi.org/10.1007/s10236-016-1021-4

Collins, C. O., III, Rogers, W. E., Marchenko, A., & Babanin, A. V. (2015). In situ measurements of an energetic wave event in the Arctic marginal ice zone. *Geophysical Research Letters*, *42*, 1863–1870. https://doi.org/10.1002/2015GL063063

Deb, K. (2001). *Multi-objective optimization using evolutionary algorithms* (518 pp.). Hoboken, NJ: John Wiley & Sons.

De Carolis, G., & Desiderio, D. (2002). Dispersion and attenuation of gravity waves in ice: A two-layer viscous fluid model with experimental data validation. *Physical Letters A*, *305*, 399–412.

De Carolis, G., Olla, P., & Pignagnoli, L. (2005). Effective viscosity of grease ice in linearized gravity waves. *Journal of Fluid Mechanics*, *535*, 369–381. https://doi.org/10.1017/S002211200500474X

Doble, M. J., De Carolis, G., Meylan, M. H., Bidlot, J.-R., & Wadhams, P. (2015). Relating wave attenuation to pancake ice thickness, using field measurements and model results. *Geophysical Research Letters*, *42*, 4473–4481. https://doi.org/10.1002/2015GL063628

Fox, C., & Squire, V. A. (1994). On the oblique reflexion and transmission of ocean waves at shore fast sea ice. *Philosophical Transactions of Royal Society of London A*, *347*, 185–218. https://doi.org/10.1098/rsta.1994.0044

Frankenstein, S., Løset, S., & Shen, H. H. (2001). Wave–ice interactions in Barents Sea marginal ice zone. *Journal of Cold Regions Engineering*, *15*(2), 91–102.

Greenhill, A. G. (1887). Wave motion in hydrodynamics. *American Journal of Mathematics*, *9*, 62–112.

Groves, J. E., & Stringer, W. J. (1991). The use of AVHRR thermal infrared imagery to determine sea ice thickness within the Chukchi polynya. *Arctic*, *44*, 130–139. Retrieved form http://www.jstor.org/stable/40510990

Hartigan, J. A. (1975). *Clustering algorithms* (351 pp.). New York: John Wiley and Sons, Inc.

Hasselmann, K., Barnett, T., Bouws, P., Carlson, E. H., Cartwright, D., Enke, E. K., . . . Walden, H. (1973). *Measurements of wind-wave growth and swell decay during the Joint North Sea Wave Project (JONSWAP)* (93 pp.). Deutches Hydrographisches Institut. Retrieved from uuid: f204e188-13b9–49d8-a6dc-4fb7c20562fc

Hasselmann, S., Hasselmann, K., Allender, J. H., & Barnett, T. P. (1985). Computations and parameterizations of the nonlinear energy transfer in a gravity-wave specturm. Part II: Parameterizations of the nonlinear energy transfer for application in wave models. *Journal of Physical Oceanography*, *15*(11), 1378–1391.

Hebert, D. A., Allard, R. A., Metzger, E. J., Posey, P. G., Preller, R. H., Wallcraft, A. J., . . . Smedstad, O. M. (2015). Short-term sea ice forecasting: An assessment of ice concentration and ice drift forecasts using the U.S. Navy's Arctic Cap Nowcast/Forecast System. *Journal of Geophysical Res.: Oceans*, *120*, 8327–8345. https://doi.org/10.1002/2015JC011283

Herbers, T. H. C., Jessen, P. F., Janssen, T. T., Colbert, D. B., & MacMahan, J. H. (2012). Observing ocean surface waves with GPS-tracked buoys. *Journal of Atmospheric and Oceanic Technology*, *29*, 944–959.

Hogan, T. *et al.* (2014). The Navy Global Environmental Model. *Oceanography*, *27*(3), 116–125.

Huang, Z. (1998). Extensions to the k-means algorithm for clustering large data sets with categorical values. *Data Mining and Knowledge Discovery*, *2*, 283–304. https://doi.org/10.1023/A:1009769707641

Hunkins, K. (1962). Waves on the Arctic ocean. *Journal of Geophysical Research*, *67*(6), 2477–2489. https://doi.org/10.1029/JZ067i006p02477

Huntemann, M., Heygster, G., Kaleschke, L., Krumpen, T., Mäkynen, M., & Drusch, M. (2014). Empirical sea ice thickness retrieval during the freeze up period from SMOS high incident angle observations. *The Cryosphere*, *8*(2), 439–451.

Keller, J. B. (1998). Gravity waves on ice-covered water. *Journal of Geophysical Research*, *103*(C4), 7663–7669.

Kohout, A. L., Penrose, B., Penrose, S., & Williams, M. J. M. (2015). A device for measuring wave-induced motion of ice floes in the Antarctic marginal ice zone. *Annals of Glaciology*, *56*(69). https://doi.org/10.3189/2015AoG69A600

Kohout, A. L., Williams, M. J. M., Dean, S. M., & Meylan, M. H. (2014). Storm-induced sea-ice breakup and the implications for ice extent. *Nature*, *509*(7502), 604–607. https://doi.org/10.1038/nature13262

Komen, G. J., Cavaleri, L., Donelan, M., Hasselmann, K., Hasselmann, S., & Janssen, P. A. E. M. (1994). *Dynamics and modelling of ocean waves* (532 pp.). Cambridge, UK: Cambridge Univ. Press.

Komen, G. J., Hasselmann, K., & Hasselmann, K. (1984). On the existence of a fully developed wind-sea spectrum. *Journal of Physical Oceanography*, *14*(8), 1271–1285.

Kramer, H. J. (1996). *Observation of the earth and its environment: Survey of missions and sensors* (3rd ed., 805 pp.). Berlin, Germany: Springer. https://doi.org/10.1007/978-3-642-97678-0

Kuik, A. J., Van Vledder, G. P., & Holthuijsen, L. H. (1988). A method for the routine analysis of pitch-and-roll buoy wave data. *Journal of Physical Oceanography*, *18*, 1020–1034.

LeSchack, L. A., & Haubrich, R. A. (1964). Observations of waves on an ice-covered ocean. *Journal of Geophysical Research*, *69*(8), 3815–3821. https://doi.org/10.1029/JZ069i018p03815

Li, J., Kohout, A. L., & Shen, H. H. (2015). Comparison of wave propagation through ice covers in calm and storm conditions. *Geophysical Research Letters*, *42*, 5935–5941. https://doi.org/10.1002/2015GL064715

Liu, A. K., & Mollo-Christensen, E. (1988). Wave propagation in a solid ice pack. *Journal of Physical Oceanography*, *18*, 1702–1712.

Longuet-Higgins, M. S., Cartwright, D. E., & Smith, N. D. (1963). *Observations of the directional spectrum of sea waves using the motions of a floating buoy Ocean Wave Spectra* (pp. 111–136). NJ: Prentice-Hall. https://doi.org/10.1016/0011-7471(65)91457-9

Marchenko, A., & Cole, D. (2017). Three physical mechanisms of wave energy dissipation in solid ice, Paper presented at 24th International Conference on Port Ocean Engineering under Arctic Conditions, June 11–16.

Marchenko, A., Rabault, J., Sutherland, G., Collins, C. O., III,Wadhams, P., & Chumakov, M. (2017). Field observations and preliminary investigations of a wave event in solid drift ice in the Barents Sea. Paper presented at 24th International Conference on Port Ocean Engineering under Arctic Conditions, Busan, Korea, June 11–16.

Markus, T., & Cavalieri, D. J. (2000). An enhancement of the NASA Team sea ice algorithm. *IEEE Transactions on Geoscience and Remote Sensing*, *38*(3), 1387–1398.

Markus, T., & Cavalieri, D. J. (2009). The AMSR-E NT2 sea ice concentration algorithm: Its basis and implementation. *The Remote Sensing Society of Japan*, *29*(1), 216–225.

Mei, C. C., Krotov, M., Huang, Z., & Huhe, A. (2010). Short and long waves over a muddy seabed. *Journal of Fluid Mechanics*, *643*, 33–58. https://doi.org/10.1017/S0022112009991923

Melia, N., Haines, K., & Hawkins, E. (2016). Sea ice decline and 21st century trans-Arctic shipping routes. *Geophysical Research Letters*, *43*, 9720–9728. https://doi.org/10.1002/2016GL069315

Meyers, M. A., & Chawla, K. K. (2008). *Mechanical behavior of materials* (pp. 689–690). Cambridge, UK: Cambridge University Press.

Meylan, M. H., Bennetts, L. G., & Kohout, A. L. (2014). In situ measurements and analysis of ocean waves in the Antarctic marginal ice zone. *Geophysical Research Letters*, *41*, 5046–5051. https://doi.org/10.1002/2014GL060809

Mosig, J. E. M., Montiel, F., & Squire, V. A. (2015). Comparison of viscoelastic-type models for ocean wave attenuation in ice-covered seas. *Journal of Geophysical Research: Oceans*, *120*, 6072–6090. https://doi.org/10.1002/2015JC010881

Murata, T., & Ishibuchi, H. (1995). MOGA: Multi-objective genetic algorithms. Presented at IEEE International Conference on Evolutionary Computation (Vol. 1, p. 289). https://doi.org/10.1109/ICEC.1995.489161

Newyear, K., & Martin, S. (1999). Comparison of laboratory data with a viscous two-layer model of wave propagation in grease ice. *Journal of Geophysical Research*, *104*(C4), 7837–7840. https://doi.org/10.1029/1999JC900002

Palmer, A., & Croasdale, K. (2012). *Arctic offshore engineering* (357 pp.). Singapore: World Scientific Pub. Co.

Peters, A. S. (1950). The effect of a floating mat on water waves. *Communications on Pure and Applied Mathematics*, *3*, 319–354.

Posey, P. G., Metzger, E. J., Wallcraft, A. J., Hebert, D. A., Allard, R. A., Smedstad, O. M., . . . Helfrich, S. R. (2015). Improving Arctic sea ice edge forecasts by assimilating high horizontal resolution sea ice concentration data into the US Navy's ice forecast systems. *The Cryosphere*, *9*, 1735–1745. https://doi.org/10.5194/tc-9-1735-2015

Rabault, J., Sutherland, G., Gundersen, O., & Jensen, A. (2017). Measurement of wave damping by a grease ice slick in Svalbard using off-the-shelf sensors and open-source electronics. *Journal of Glaciology*, *63*(238), 372–381. https://doi.org/10.1017/jog.2017.1

Rogers, W. E., Thomson, J., Shen, H. H., Doble, M., Wadhams, P., & Cheng, S. (2016). Dissipation of wind waves by pancake and frazil ice in the autumn Beaufort Sea. *Journal of Geophysical Research: Oceans*, *121*, 7991–8007. https://doi.org/10.1002/2016JC012251

Sakai, S., & Hanai, K. (2002). Empirical formula of dispersion relation of waves in sea ice. In *Proceedings of 16th IAHR international symposium on Ice in the environment* (pp. 327–335).

Smith, M. M., Thomson, J., Stammerjohn, S. E., Persson, O. P. G., & Rainville, L. (2016). Observations of wave-enhanced mixing in the autumn Arctic Ocean. Moscone South, San Francisco, CA: AGU Fall Meeting, Poster C21C-0695, Dec. 13, 2016. Retrieved from https://agu.confex.com/agu/fm16/meetingapp.cgi/Paper/142630

Snyder, R. L., Dobson, F. W., Elliott, J. A., & Long, R. B. (1981). Array measurements of atmospheric pressure fluctuations above surface gravity waves. *Journal of Fluid Mechanics*, *102*, 1–59.

Squire, V. A. (2007). Of ocean waves and sea-ice revisited. *Cold Regions Science Technology*, *49*(2), 110–133.

Squire, V. A. (2011). Past, present and impendent hydroelastic challenges in the polar and subpolar seas. *Philosophical Transactions of Royal Society A*, *369*, 2813–2831. https://doi.org/10.1098/rsta.2011.0093

Squire, V. A., & Allan, A. J. (1980). Propagation of flexural gravity waves in sea ice, in Sea Ice Processes and Models. In R. S. Pritchard (Ed.), *Proceedings of Arctic Ice Dynamics Joint Experiment* (pp. 327–338). Seattle, WA: University of Washington Press.

Squire, V. A., & Montiel, F. (2016). Evolution of directional wave spectra in the marginal ice zone: A new model tested with legacy data. *Journal of Physical Oceanography*, *46*, 3121–3137. https://doi.org/10.1175/JPO-D-16-0118.1

Squire, V. A., & Moore, S. C. (1980). Direct measurement of the attenuation of ocean waves by pack ice. *Nature*, *283*, 365–368.

Squire, V. A., Robinson, W. H., Meylan, M., & Haskell, T. G. (1994). Observations of flexural waves on the Erebus ice tongue, McMurdo Sound, Antarctica, and nearby sea ice. *Journal of Glaciology*, *40*(135), 377–385. https://doi.org/10.3198/1994JoG40-135-377-385

Thomson, J. (2012). Observations of wave breaking dissipation with SWIFT drifters. *Journal of Atmospheric Oceanic Technology*. https://doi.org/10.1175/JTECH-D-12-00018.1

Thomson, J. (2015). *ONR Sea State DRI Cruise Report: R/V Sikuliaq, Fall 2015 (SKQ201512S)* (45 pp.), Seattle, WA: University of Washington.

Thomson, J., Ackley, S., Shen, H. H., & Rogers, W. E. (2017). The balance of ice, waves, and winds in the Arctic autumn. *Eos Trans. AGU*, *98*, https://doi.org/10.1029/2017EO066029

Thomson, J., De Klerk, A., Brown, A., Schwendeman, M., Goldsmith, J., Thomas, J., . . . Meinig, C. (2015). Biofouling effects on the response of a wave measurement buoy in deep water. *Journal of Atmospheric Oceanic Technology*, *32*, 1281–1286. https://doi.org/10.1175/JTECH-D-15-0029.1

Thomson, J., & Rogers, W. E. (2014). Swell and sea in the emerging Arctic Ocean. *Geophysical Research Letters*, *41*, 3136–3140. https://doi.org/10.1002/2014GL059983

Timco, G. W., & Weeks, W. F. (2010). A review of the engineering properties of sea ice. *Cold Regions Science Technology*, *60*, 107–129. https://doi.org/10.1016/j.coldregions.2009.10.003

Tolman, H. L. (2003). Treatment of unresolved islands and ice in wind wave models. *Ocean Modelling*, *5*(3), 219–231. https://doi.org/10.1016/S1463-5003(02)00040-9

Tolman, H. L., & Chalikov, D. (1996). Source terms in a third-generation wind wave model. *Journal of Physical Oceanography*, *26*(11), 2497–2518. Retrieved from http://journals.ametsoc.org/doi/pdf/10.1175/1520-0485%281996%29026%3C2497%3ASTIATG%3E2.0.CO%3B2

Tolman, H. L., & the WAVEWATCH III® Development Group (2016). *User manual and system documentation of WAVEWATCH III® version5.16* (NOAA Tech. Note MMAB Contribution 329, 361 pp.)

Wadhams, P. (1973). Attenuation of swell by sea ice. *Journal of Geophysical Research*, *78*(18), 3552–3563. https://doi.org/10.1029/JC078i018p03552

Wadhams, P. (1986). The seasonal ice zone. In N. Untersteier (Ed.), *The geophysics of sea ice* (pp. 825–991). New York: Plenum.

Wadhams, P., & Holt, B. (1991). Waves in frazil and pancake ice and their detection in Seasat synthetic aperture radar imagery. *Journal of Geophysical Research*, *96*(C5), 8835–8852.

Wadhams, P., Parmiggiani, F., & De Carolis, G. (2002). The use of SAR to measure ocean wave dispersion in frazil-pancake icefields. *Journal of Physical Oceanography*, *32*, 1721–1746. https://doi.org/10.1175/1520-0485(2002)032 < 1721:TUOSTM>2.0.CO;2

Wadhams, P., Parmiggiani, F., De Carolis, G., Desiderio, D., & Doble, M. (2004). SAR imaging of wave dispersion in Antarctic pancake ice and its use in measuring ice thickness. *Geophysical Research Letters*, *31*, L15305. https://doi.org/10.1029/2004GL020340

Wadhams, P., Squire, V. A., Ewing, J. A., & Pascal, R. W. (1986). The effect of the marginal ice zone on the directional wave spectrum of the ocean. *Journal of Physical Oceanography*, *6*(2), 358–376.

Wadhams, P., Squire, V. A., Goodman, D. J., Cowan, A. M., & Moore, S. C. (1988). The Attenuation Rates of Ocean Waves in the Marginal Ice Zone. *Journal of Geophysical Research*, *93*(C6), 6799–6818.

Wadhams, P., & Thomson, J. (2015). The Arctic Ocean cruise of R/V Sikuliaq 2015, An investigation of waves and the advancing ice edge. *Il Polo*, *LXX-4*, 9–38.

Wang, R., & Shen, H. H. (2010). Gravity waves propagating into ice-covered ocean: A visco-elastic model. *Journal of Geophysical Research*, *115*, C06024. https://doi.org/10.1029/2009JC005591

Wang, X., Key, J. R., & Liu, Y. (2010). A thermodynamic model for estimating sea and lake ice thickness with optical satellite data. *Journal of Geophysical Research: Oceans*, *115*, C12035. https://doi.org/10.1029/2009JC005857

WAVEWATCH III® Development Group (2016). *User manual and system documentation of WAVEWATCH III® version 5.16* (361 pp.).

Weber, J. E. (1987). Wave attenuation and wave drift in the marginal ice zone. *Journal of Physical Oceanography*, *17*, 2351–2361.

Weitz, M., & Keller, J. B. (1950). Reflection of water waves from floating ice in water of finite depth. *Communications of Pure and Applied Mathematics*, *3*, 305–318.

Wu, J. (1982). Wind-stress coefficients over sea surface from breeze to hurricane. *Journal of Geophysical Research: Oceans*, *87*(C12), 9704–9706. https://doi.org/10.1029/JC087iC12p09704

Young, I. R. (1995). The determination of confidence limits associated with estimates of the spectral peak frequency. *Ocean Engineering*, *22*(7), 669–686.

Young, I. R., Rosenthal, W., & Ziemer, F. (1985). A three dimensional analysis of marine radar images for the determination of ocean wave directionality and surface currents. *Journal Geophysical Research*, *90*(C1), 1049–1059. https://doi.org/10.1029/JC090iC01p01049

Yu, Y., & Rothrock, D. A. (1996). Thin ice thickness from satellite thermal imagery. *Journal of Geophysical Research: Oceans*, *101*(C11), 25753–25766.

Zhao, X., Cheng, S., & Shen, H. H. (2017). Nature of wave modes in coupled viscoelastic layer over water. *Journal of Engineering Mechanics*, *143*(10), 04017114. https://doi.org/10.1061/(ASCE)EM.1943-7889.0001332

Zhao, X., & Shen, H. H. (2015). Wave propagation in frazil/pancake, pancake, and fragmented ice covers. *Cold Regions Science Technology*, *113*, 71–80. https://doi.org/10.1016/j.coldregions.2015.02.007

Zippel, S., & Thomson, J. (2016). Air-sea interactions in the marginal ice zone. *Elementa: Science of the Anthropocene*, *4*, 95.